FIRST-PRINCIPLES STUDIES ON N-TYPE AND P-TYPE DOPING IN CUPROUS OXIDE

by

QIONG BAI

Presented to the Faculty of the Graduate School of

The University of Texas at Arlington in Partial Fulfillment

of the Requirements

for the Degree of

DOCTOR OF PHILOSOPHY

THE UNIVERSITY OF TEXAS AT ARLINGTON

August 2012

ACKNOWLEDGEMENTS

First of all, I would like to express my deepest appreciation and gratitude to my advisor, Dr. Qiming Zhang, for guiding me into the areas of microelectronics and providing instructions and encouragement throughout my research. I also acknowledge Dr. Muhammad Huda, Dr. Fuqiang Liu, Dr. Yaowu Hao, and Dr. Jiangjie Chao for being my committee members and discussion on my dissertation.

I would also like to acknowledge my current group members, Congxin Xia and Joaquin Noyola, and my friend Xiaofei Han for their assistance, support and friendship. I am always grateful to our department secretaries, Jennifer Standlee and Lidia Cuauhtli. I appreciate their help and patience during my graduate study in UT Arlington.

Finally, I devote my deepest appreciation to my parents, my brother, and all my cousins. Without their love, support and understanding, this thesis would have been impossible.

This research was supported by the U.S. Department of Energy, Office of Basic Energy Sciences, Division of Materials Sciences and Engineering under Award No. DE-SC0002062. The computational work was done at the High Performance Computing Center of the University of Texas at Arlington.

July 19, 2012

ABSTRACT

FIRST-PRINCIPLES STUDIES ON N-TYPE AND

P-TYPE DOPING IN CUPROUS OXIDE

Qiong Bai, PhD

The University of Texas at Arlington, 2012

Supervising Professor: Qiming Zhang

We have performed studies on n-type and p-type cuprous oxide with and without doping by first principles methods. Generalized Gradient Approximation (GGA) is used for the geometry optimization. The total energy and the final electronic structure calculations are conducted using the nonlocal screened Heyd-Scuseria-Ernzerhof (HSE) hybrid density functionals approach for cuprous oxide. The HSE hybrid density functionals overcome the shortcoming of GGA, which gives a much reliable value of the band gap.

The formation energies of native point defects in undoped cuprous oxide have been studied by HSE hybrid functional theory in two conditions, which are vacuum based condition and solution based condition. Copper vacancy always has the lowest formation energy and provides p-type conductivity in both Cu-rich and O-rich conditions in vacuum based conditions. In the solution with low pH value, n-type cuprous oxide is achievable, where the antisite defect Cu_O is the dominant defect and responsible for the n-type conduction.

Various elements are used to dope in cuprous oxide. In n-type doped cuprous oxide, certain halogen atoms, i.e., F, Cl and Br, are used to substitute the O atom. The metallic atoms, i.e., Ca, Mg, and Zn, are used to substitute Cu atom. The dopant in substitutional site has lower

formation energy. Cl has the shallowest defect level among halogen atoms, which is favorable for electron to go to conduction band. In metallic atoms, Ca is the best candidate dopant with low formation energy and shallow transition level. The extra electron can be excited into bottom of conduction band. Also, the bottom of conduction band is dominated by 3s orbital of O atom, which is non-localized. The excited electron can move fast in 3s orbital and further improve the conductivity.

For p-type doping to improve the properties of the p-type material, certain group V elements, such as N, P and As, are used to substitute an O atom. In a solution with pH=9, the formation energy of nitrogen substitutional defect is lower than that of copper vacancy, which means that nitrogen substitutional defect is a dominant defect and provides more free carriers, and further improves the conductivity of cuprous oxide. From the consideration of both the formation energy and the donor level, N is the best dopant among these three dopants.

Finally, n-type doping in ZnO by Y has been studied. Oxygen vacancies, zinc interstitials, and zinc substitution by Y are considered here. We considered the formation energy of defects from two limit conditions, which are Zn-rich and O-rich. In Zn-rich condition, copper vacancy has the lowest formation energy. In O-rich condition, yttrium substitutional has the lowest formation energy and is a dominant defect, which will decrease the resistivity of ZnO.

TABLE OF CONTENTS

ACKNOWLEDGEMENTS iii

ABSTRACT iv

LIST OF ILLUSTRATIONS ix

LIST OF TABLES xi

Chapter Page

1. INTRODUCTION 1

1.1 Energy Consumption 1

1.2 Renewable Energy 1

1.3 Solar Energy and Solar Cell 2

1.4 Copper Oxide as a Solar Cell Material 5

1.5 Zinc Oxide as an Anti-reflective Coating 6

1.6 Development of Computational Science 7

1.7 Research Objectives 7

2. METHODOLOGY 10

2.1 Density Functional Theory 10

2.1.1 Born-Oppenheimer Approximation 11

2.1.2 Thomas-Fermi-Dirac Approximation 13

2.1.3 Hohenberg-Kohn Theorems 14

2.1.4 Kohn-Sham Equation 17

2.1.5 Local Density Approximation 19

2.1.6 Generalized Gradient Approximation 21

2.1.7 Hybrid Functional 22

2.2 Plane Wave Basis Sets and Pseudopotential Approximation 23

2.2.1 Plane Wave Basis Sets 23
2.2.2 Pseudopotential Approximation 25
2.2.3 Solution of Kohn-Sham Equation 27
2.3 Formation Energy of Defect 30
3. UNDOPED CUPROUS OXIDE..... 32
3.1 Introduction 32
3.2 Crystal Structure 34
3.3 Computational Details 35
3.4 Structural and Electronic Properties 36
3.5 Formation Energies of Native Point Defects 38
3.5.1 Formation Energies in Vacuum Conditions 39
3.5.2 Formation Energies in Solution Conditions 41
3.6 Summary 45
4. N-TYPE DOPING IN CUPROUS OXIDE 47
4.1 Introduction 47
4.2 Computational Details 48
4.3 Formulas of Formation Energy and Determination of pH Value 48
4.4 N-type Doping in Cu_2O by Halogen Atoms 49
4.4.1 Structural and Electronic Properties 49
4.4.2 Calculation of Formation Energies 51
4.5 N-type Doping in Cu_2O by Selected Metal Atoms 55
4.5.1 Structural and Electronic Properties 55
4.5.2 Formation Energies in Vacuum Conditions 56
4.5.3 Formation Energies in Solution Conditions 57
4.6 N-type Co-doping in Cu_2O by Cl and Ca 59

4.7 Summary 61

5. P-TYPE DOPING IN CUPROUS OXIDE 63

5.1 Introduction 63

5.2 Computational Details 64

5.3 Structural Properties 64

5.4 Determination of the Chemical Potential 65

5.4.1 How to Determine the Chemical Potential of Cu 65

5.4.2 How to Determine the Chemical Potential of Group V atoms 65

5.5 Calculation of Formation Energies 67

5.6 Summary 69

6. N-TYPE DOPING IN ZINC OXIDE BY YTTRIUM 70

6.1 Introduction 70

6.2 Computational Details 70

6.3 Calculation of Formation Energies 71

6.4 Summary 74

7. CONCLUSION 75

REFERENCES 78

BIOGRAPHICAL INFORMATION 85

LIST OF ILLUSTRATIONS

Figure Page

1.1 Schematic figure of principle of solar cell 3

1.2 The development of efficiency of solar cells 4

2.1 Comparison between pseudopotential and real potential 26

2.2 Self-consistent calculation flow chart 29

3.1 Crystal structure of Cu_2O. Deep red balls represent oxygen atoms, while pink ones copper atoms 35

3.2 Electronic band structure of native Cu_2O. The energy level of valence band maximum corresponds to the zero energy 37

3.3 Density of state of Cu_2O by Hybrid functional (left) and GGA (right) 38

3.4 Formation energies as a function of Fermi level of native point defects in Cu_2O under (a) O-rich and (b) Cu-rich conditions in vacuum based growth. The zero point of the Fermi level corresponds to the top of the valence band. Only segments corresponding to the lowest-energy charge states are shown. The slope of these segments indicates the charge. Kinks in the curves indicate transitions between different charge states. 40

3.5 The range of chemical potential of Cu (a) at vacuum condition, (b) at solution condition. (a) The two limit values are obtained at Cu-rich and O-rich conditions. (b) The two limit values are obtained at pH=0 and pH=14, which correspond to the strong acid solution and strong basic solution 43

3.6 Formation energies as a function of Fermi level for native point defects in Cu_2O in the solution with pH=9 44

3.7 Formation energies as a function of Fermi level for native point defects in Cu_2O in the solution with pH=6 44

3.8 Formation energies as a function of Fermi level for native point defects in Cu_2O in the solution with pH=4 45

4.1 Sites for high symmetric interstitial defect (T1, T2 are the tetrahedral sites and O is the octahedral site) 51

4.2 Formation energies of defects of Cu_2O as a function of Fermi level at pH=4. Formation energies of F, Cl, and Br at neutral and charge=+1 are given in panel a, b and c, respectively. And the formation energy of Cu

vacancy is given as dashed line in panel b. 53

4.3 The single-particle impurity levels. The single particle impurity levels of the substitutional F, Br, and Cl are shown, measured from VBM in eV. The Cl dopant has the shallowest level, about 0.17eV below the CBM 54

4.4 The projected density-of-states (DOS). The DOS of crystal Cu_2O projected by angular-momentum near the band gap are plotted VS the Fermi level, which has the zero point at theVBM. Panel (a) is for the oxygen site projection, where the s-component is amplified by 20 times. Panel (b) is for the copper site projection, where both the s- and p-components are amplified by 20 times 54

4.5 Formation energies of metal defects in Cu_2O under (a) Cu-poor/O-rich and (b) Cu-rich/O-poor conditions in vacuum based growth. The zero point of the Fermi level corresponds to the top of the valence band. Only segments corresponding to the lowest-energy charge states are shown. Kinks in the curves indicate transitions between different charge states..... 57

4.6 Formation energies of defects of Cu_2O as a function of the Fermi level at pH=6for Zn and at pH=4 for Ca and Mg. Formation energies of Zn, Ca, and Mg at neutral and charge=+1 are given in panel a, b, and c, repectively. And the formation energy of Cu vacancy is given..... 58

4.7 The single-particle impurity levels. The single particle impurity levels of the substitutional Zn, Ca, and Mg are shown, measured from VBM in eV. The Ca dopant has the shallowest level, about 0.11 eV below the CBM 59

4.8 Formation energies of Cl_O and Ca_{Cu} and Cl_O-Ca_{Cu} as a function of the Fermi level at pH=4. Formation energies of Cl_O and Ca_{Cu} at neutral and charge=+1 states are given. And Formation energy of Cl_O-Ca_{Cu} at neutral and charge=+2 states are given..... 60

5.1 The formation energies of the group V dopants. In this figure, the formation energies of the substitutional defect in Cu_2O at the basic solution-growth environment of pH=9 are plotted, respectively. They vary with the Fermi level ranging from the valence-band maximum (VBM) to the conduction-band minimum (CBM). The lowest formation energies of interstitial site for each dopant are shown in their corresponding panels. 67

5.2 The formation energies of substitutional defects at the basic solution-growth environment of pH=9 and pH=10 are plotted. They vary with the Fermi level ranging from the valence-band maximum (VBM) to the conduction-band minimum (CBM). The lowest formation energies of interstitial site for each dopant are shown in their corresponding panels. The formation energy of the p-type native defect, Cu vacancy, is shown for comparison. 68

6.1 Formation energies of defects in ZnO under (a) O-rich and (b) Zn-rich conditions in vacuum based growth. The zero point of the Fermi level corresponds to the top the of the valence band. Only the lowest-energy charge states are shown. 73

LIST OF TABLES

Table Page

3.1 Comparison of the lattice constant (a), Cu-O bond lengths, and fundamental band gaps of bulk Cu_2O from previous theoretical and experimental studies and those from the current GGA and GGA+U calculations. Bond distances and lattice parameters are given in Å and Eg is measured in eV 36

4.1 The distance of the first nearest neighbors and the change from an ideal Cu–O bond length in Cu_2O after the O substitution by halogen atoms 50

4.2 The distance of the first nearest neighbors and the change from an ideal Cu–O bond length in Cu_2O after the O substitution by metal atoms..... 55

5.1 The distance of the first nearest neighbors and the change from an ideal Cu–O bond length in Cu_2O after the substitution 65

5.2 The possible compounds and their corresponding chemical potential. 66

6.1 Calculated lattice parameters a, c/a, and band gap Eg by using GGA and LDA 71

CHAPTER 1

INTRODUCTION

1.1 Energy Consumption

As the global economy develops rapidly, the energy consumption is growing very fast annually. According to International Energy Agency (IEA), the total world energy supply was 102,569 TWh (1990); 117,687 TWh (2000); 133,602 TWh (2005) and 143,851 TWh (2008). In 2008, the energy supply by power source was oil 33.5%, coal 26.8%, gas 20.8%, renewable energy 12.9%, nuclear 5.8% and other 4% [1]. It is clearly that oil was the most popular energy fuel. Oil, coal and natural gas combined represented over 80% of the world energy supply.

Oil, coal and natural gas are called fossil fuels, which are fuels formed by natural processes such as anaerobic decomposition of buried dead organisms and usually take millions of years to form by exposure to heat and pressure. Fossil fuels range from volatile materials like methane, to liquid petroleum to nonvolatile materials composed of almost pure carbon, like anthracite coal [2-4]. The total reserves of fossils fuels on the earth are limited. In the modern world, the reserves are being depleted much faster than new ones are being made. It means that the reservation of fossil fuels will run out in the future. To meet the growing need of energy consumption in the future, we have to find some alternative energy sources to supplement fossil fuels. Also, fossil fuels are not clean energy because that large amount of carbon dioxide will be generated during fossil fuel burning, which will increase the concentration of carbon dioxide in the global environment and further lead to the global warming problem.

1.2 Renewable Energy

To overcome the shortcomings of fossil fuels, it is necessary to find some renewable resources to meet the part of the increased energy needs. A transition from nonrenewable energy to renewable energy is under way.

Renewable energy comes from natural resources, which are naturally replenished and don't take long time to form. Renewable energy exists as various forms. The mainstream forms of renewable energy include wind power, hydropower, solar energy, biomass, biofuel, and geothermal energy. The share of renewables in electricity generation is around 19%, with 16% coming from the hydroelectricity and 3% from other renewable sources [5]. Only a small part of wind and solar energies have been utilized. However, wind and solar radiation account for the most of the available renewable energy on the earth, which are very promising energies to harness. Recently, governments around the world become to realize the importance of these energies, and try to utilize them to meet the energy needs. The utilization of renewable energy is growing rapidly. Wind power is growing at the rate of 20% annually, with a worldwide installed capacity of 198 gigawatts (GW) in 2010 [6]. Since 2004, solar energy passed wind energy as the fastest growing energy source, and since 2007 has more than doubled every two years [7]. The solar energy is mostly utilized by solar cells (photovoltaic cells). For solar cells, the cumulative global photovoltaic installation, which is a device that converts light into electric current, have already surpassed 40 GW at the end of 2010 [7-8].

1.3 Solar Energy and Solar Cell

The Earth receives 174 petawatts (PW) of incoming solar radiation at the upper atmosphere [44]. Approximately 30% is reflected back to space while the rest is absorbed by clouds, oceans and land masses. The total solar energy absorbed by Earth's atmosphere, oceans and land masses is approximately 3,850,000 exajoules (EJ) per year [7], which one hour supply is more than the world used in one year. If only a small part of solar energy can be utilized, then our energy need in the future will be meet.

Solar radiation energy could be usually transformed to electricity by solar cells. The work principle of solar cell is based on the photovoltaic (PV) effect, which was first recognized in 1839 by Becquerel. It states that an electron in the valence band of a semiconductor can be exited into conduction band by absorbing a photon and become a free carrier. Figure 1.1 shows

the principle of a PV cell. When a p-type and n-type semiconductors are contacted each other, electrons from the n-type semiconductor diffuse into the p-type side, leaving holes behind, until enough electrons accumulate on the p-type side of the boundary and enough holes accumulate on the n-type side of the boundary that the Fermi level (Ef) on both sides are aligned, and the equilibrium is reached. Photons are then absorbed within the p-type semiconductor, exciting electrons up to conduction bands and then flowing through the p-n junction to the electrical contact, while the hole goes the other way. The electrons will go into the circuit and do work before recombination with the holes. To excite one electron, the energy of the photon must be equal to or greater than that of band gap (Ec - Ev). The remaining energy of the photon with energy higher than that of the band gap will be lost as a form of heat. The photon with energy lower than that of band gap will not be absorbed.

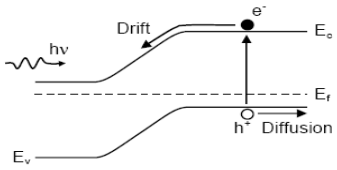

Figure 1.1 Schematic figure of principle of solar cell

At the beginning, the application of solar cell is very limited due to the high cost and low efficiency. The first photovoltaic cell was built by Charles Fritts in 1883 with efficiency around 1%. Until 1954, Daryl Chapin developed the first modern photovoltaic cell with high efficiency at Bell Laboratories [9], by using a diffused silicon p-n junction [10]. The cost of the electricity was very high with $250 per watt. In the late 1960s, Elliot Berman [10] investigated a new method for producing the silicon feedstock in a ribbon process to lower the cost to $10 per watt.

We can see that the developments of efficiency of different kinds of solar cells in the last couples of decades are shown in Figure 1.2. As it shows, the efficiency of all solar cell materials have been improved. For example, the efficiency of single crystal silicon, which is the most popular material for solar cell, has been increased up to 25% reported by University of

New South Wales [11]. The development of efficiency of multicrystalline Si and amorphous Si are also shown in Figure 1.2. Their efficiency is lower than that of single crystal Si. Actually, the theoretical efficiency of the silicon solar cell is 35.4% calculated from the band gap of silicon [12]. Therefore, there is room that the efficiency of Si solar cell still can be improved in future.

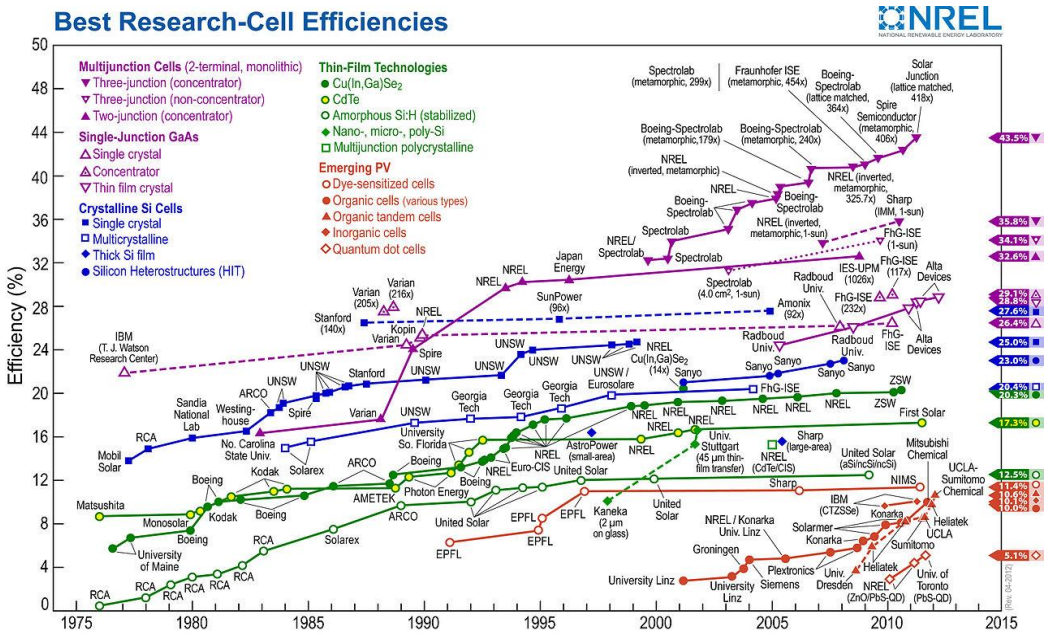

Figure 1.2 The development of efficiency of solar cells [47]

The efficiency of solar cells strongly depends on band gaps and band structures. It is shown that semiconductors with band gap between 1.4 eV have the greatest potential to form an efficient cell. Although crystal silicon has a 1.1 eV band gap, its band gap is an indirect band gap, which affects the absorption coefficient and the efficiency of solar cell. This is because that an extra phonon is needed to keep momentum conservation during the process of electron excitation by photon.

Although silicon is the second most abundant element in the world, it is always combined with other element like SiO_2 in natural and takes too much energy to purify silicon from silicon compounds. All these factors make the price of silicon crystal solar cell very high, which limit it to be massively used in solar cell industry.

In addition to crystal Si, other materials for solar cells have recently been making

significant appearance, which is economically competitive to single crystal silicon technology. These materials include CIGS (Copper indium gallium diselenide), polycrystalline Si, CdTe and so on. But these solar cell materials have disadvantages like high cost material, toxic material or poor efficiency stabilization. All these factors limit the utilization of these materials.

1.4 Copper Oxide as a Solar Cell Material

Due to high cost, toxicity, and poor stability of above materials, new solar cell materials are being searched to overcome those disadvantages, such as semiconducting metal oxides. Their constituent metallic elements are usually abundant in the earth and not harmful environmentally. Also, most importantly, they can be fabricated through wet chemistry which lowers the cost of production. As two typical examples, cupric oxide (CuO) and cuprous oxide (Cu_2O) have been studied extensively. In consideration of the solar spectrum characteristics, an ideal semiconductor for PV cells should have a band gap around 1.4 eV. CuO has a reported experimental band gap at 1.2~1.9 eV [13-14], which is a very promising material for solar cell. However, CuO is a semiconductor with an indirect band gap, which affects the absorption coefficient and the efficiency of solar cells. This is because that an extra phonon is needed to keep momentum conservation during the process of electron excitation by a photon.

On the other hand, Cu_2O is a material with direct band gap at about 2.1 eV [15-17]. Also, Cu is one of the most abundant elements in the world. Cu_2O film can be made by wet chemistry, such as electrochemical deposition [18-19], which make the fabrication low-cost. All these advantages make Cu_2O possible as a good solar cell material. Researchers conducted many experiments on Cu_2O [21-23, 45]. At the beginning, the efficiency in experiment is very low, even though the theoretical efficiency of Cu_2O is ~19% [20]. Increasing the efficiency have been a long term and slow process.

First, Cu_2O is naturally a p-type material [21], which prevents to form a p-n junction of Cu_2O. But the homojunction is the basic structure in most inorganic solar cell. Siripala [22] reports that n-type Cu_2O can be fabricated in low pH solution by electrochemical deposition.

Recently, L. Wang et al. [23] demonstrated and obtained a p-n homojunction experimentally. Although an intrinsic n-type and p-n junction of Cu_2O can be obtained, the conductivity is still very low and so is the efficiency. To further improve the conductivity of Cu_2O and hence the efficiency of the p-n junction, doping of shallow level impurities is a natural option. This has been demonstrated recently by electrochemical doping with Cl in n-type Cu_2O [25]. The experiment showed that the resistivity of Cu_2O was reduced by 5 orders of magnitude after Cl-doping. Researchers also attempted to substitute the Cu by selective metal atom, such as Zn, Mg, and so on. In 2003, Kale et al. [26] used Co and Zn and other elements co-doping in Cu_2O and found that co-doping with Zn causes decrease in resistivity. For p-type doping in Cu_2O, Ishizuka et al. [34] deposited the N doped Cu_2O by reactive radio-frequency magnetron sputtering in 2001. In their experiments, they claimed that nitrogen has the effect of increasing holes density and to generate an acceptor level of 0.14 eV above the top valence band.

1.5 Zinc Oxide as an Anti-reflective Coating

To increase the photon absorption of solar cell, the anti-reflective (AR) coating [27] on the top surface of the solar cell is necessary. Zinc oxide (ZnO) is usually used as transparent conductive oxide (TCO) which coated on the top surface of solar cell. Intrinsically, ZnO is an n-type semiconductor with a 3.3 eV band gap [30]. Its source materials, Zn and O, are naturally abundant. ZnO can be used as a popular transparent conducting oxide (TCO) [29], which offers low resistivity and high transmittance. Also, Zn and O are non-toxic. All of these advantages make ZnO an ideal material for TCO in terawatt-scale solar cells.

To act as a good AR coating, ZnO should have low resistance and high transmittance [27-28]. Since undoped ZnO is highly resistive with carrier concentrations in the 1017 m^{-3} range [31], doping is needed to bring down the resistivity. In this dissertation, we focus on a Group IIIB element, yttrium (Y), which acts as an n-type candidate dopant in ZnO. Y is an abundant element and its reserve on the planet is 610,000 tons [29], which is helpful for large scale production of solar cell. Theoretically, Y has one more valence electron than Zn in the

outmost shell, which will provide extra electron and reduce the resistivity. Experimentally, X. Han [32] and S. H. Mohamed [33] reported that the Y dopant decreases the electrical resistivity of ZnO.

1.6 Development of Computational Science

Since the 1940s, the computer technology has undergone profound development. As a platform for process automation, electronic communications, equipment control, and especially for numerical computation, the development of computer technology has promoted the development on its application. Moreover, this trend of increase on calculation speed will continue. In 1965, Intel co-founder Gordon E. Moore noted [46] that the number of components in integrated circuits had doubled every year from the invention of the integrated circuit in 1958 until 1965 and predicted that the trend would continue for at least ten years. His prediction on the development of computer power has proved to be pretty accurate. In addition to the significantly increasing computing speed in a single processor, the rapid development in network technology makes parallel computing more and more popular. This furthermore enhances the computational power.

The rapid development of computer power has promoted the development of computational sciences, which made the study of complicated materials by first-principles possible. Density Functional Theory (DFT) [35-36] is an important theoretical basis for first-principles calculations. With a high speed of computing power, DFT-based methods have demonstrated its power in the study of the ground state properties of materials, including structural, electronic, and magnetic properties. The rapid development of computing facility and theoretical algorithms make modeling and simulations to be powerful in study of even complicated system. In the past decade, some computer programing packages have been developed to perform quantum mechanical calculations on various materials, such as WIEN2K, VASP, CASTEP and Quantum Espresso.

1.7 Research Objectives

In this dissertation, the first principles method will be used to study various doping in oxides, mostly in Cu_2O. In the present work, the density functional with generalized gradient approximation (GGA) [64] and Heyd-Scuseria-Ernzerhof (HSE) hybrid functional [42-43] will be applied to the study of the structural, electronic properties and formation energies. In Chapter 3, the structural and electronic properties of pure Cu_2O will be studied by DFT-GGA and HSE. Firstly, the pseudopotentials of atoms will be tested by comparing the calculated value and experimental value of lattice constant. Also, the band gaps calculated by GGA and HSE will be compared. It is well known that GGA underestimates the band gap which is well lower than the experimental value. On the other side, HSE give a more accurate band gap, which is important in deciding the impurity level in the band gap. Here, HSE will mainly be used in the following research on the electronic structures of Cu_2O.

Intrinsically, Cu_2O is a p type semiconductor [87-90], in which copper vacancy is a dominant defect and provides the conductivity. In Chapter 3, the formation energies of native defects will be considered in both of vacuum condition and solution condition. The pH dependence of defect formation will be studied to understand how pH value affects the conductivity of Cu_2O. In Chapter 4, the n-type doping in Cu_2O by halogen atoms and selective metal atoms will be studied. The halogen atoms refer to fluorine (F), chlorine (Cl), and bromine (Br), which are used to substitute the O atom. Another alternative n-type doping is to substitute Cu atom by metal atoms, which are calcium (Ca), magnesium (Mg), and zinc (Zn). Besides single doping by either halogen atoms or metal atoms, co-doping will be also considered to compare with single element doping. In Chapter 5, p-type doping in Cu_2O by group V elements, which are nitrogen (N), phosphorus (P), and arsenic (As), is studied for the p-type conductivity of Cu_2O. The conductivity of intrinsic Cu_2O is mainly provided by copper vacancy, which is via a polaronic, hole-hopping mechanism [104-106] with a poor mobility. Here, we attempt to improve the p-type conductivity of Cu_2O by providing free carriers by group V dopants.

In Chapter 6, yttrium (Y) doped ZnO will be studied by GGA to analyze the formation

energy of intrinsic defects and Y defect. The conclusion will be given in Chapter 7.

CHAPTER 2

METHODOLOGY

First-principles calculations are used to study the structural and electronic properties of materials, which refer to quantum mechanical calculations without any external parameters except the atomic numbers of the atoms in the calculations. In this chapter, the theoretical background of density functional theory, which is based on first-principles, the approximations used for practical calculations, and various methods implemented are described. Also, plane wave basis sets and pseudopotential approximation are described in this chapter. Formation energy of defect is an important research topic in this dissertation. The methods and equations are used to calculate formation energy.

2.1 Density Functional Theory

Density functional theory (DFT) has been widely used in computational physics, computational chemistry, and computational materials to describe properties of condensed matter systems during the last couples of decades. DFT can be used in calculation of standard bulk materials, interfaces, nanoparticles, and so on. DFT is used to describe a many body interacting system via its charge density, which will reduce the many body system to one body system through its charge density. Hohenberg-Kohn theorem [35] is the fundamental theoretical basis of DFT, which states that all properties of a system can be considered to be unique functionals of its ground state density. Together with the Born-Oppenheimer approximation [48] and Kohn-Sham equation [36], practical accurate DFT calculations have been made possible via approximations for the exchange-correlation (XC) potential, which describes the many body effects, which include Pauli principle and the Coulomb potential beyond a pure interaction of the electrons. Because the XC energy cannot be calculated exactly, some approximations are used, which include local density approximation (LDA), generalized gradient approximation

(GGA) and hybrid functional. LDA is the first and widely used approximation, which treats that the XC energy density at a point is the same as that of a homogeneous electron gas. GGA incorporates density gradient correction, which make an improvement on LDA.

With these approximations for the XC energy functional, the results of DFT calculations for many body systems is in a good agreement experimental results for many materials. In comparison with Hartree-Fock theory [49], LDA and GGA save a lot of time on calculation. However, they always underestimate the band gap of material.

There are still difficulties in using DFT to properly describe intermolecular interactions; charge transfer excitations; transition states, global potential energy surfaces and some other strongly correlated systems [50], especially in calculations of the band gap of some semiconductors. Recently, hybrid density functional, which incorporates exact exchange by combining Hartree-Fock, is often used to study the properties of materials. This method has further improved upon the DFT results.

2.1.1 Born-Oppenheimer Approximation

Born-Oppenheimer approximation is a very important approximation used to simplify the calculation. In this approximation, the Hamiltonian of a many-body system consisting of nuclei and electrons can be expressed as:

$$\hat{H} = \hat{T} + \hat{V}, \tag{2.1.1}$$

where $\hat{T}$ is the total kinetic energy and $\hat{V}$ is the total potential energy.

$$\hat{T} = -\sum_{I}^{N} \frac{\hbar^2}{2M_I} \nabla_{R_I}^2 - \sum_{i}^{n} \frac{\hbar^2}{2m_e} \nabla_{r_i}^2, \tag{2.1.2}$$

where the first term is the kinetic energy of the nuclei, and the second term is the kinetic energy of the electrons.

$$\hat{V} = \frac{1}{2}\sum_{I=1}^{N}\sum_{\substack{J=1 \\ J\neq I}}^{N} \frac{Z_I Z_J e^2}{|R_I - R_J|} + \frac{1}{2}\sum_{i=1}^{n}\sum_{\substack{j=1 \\ j\neq i}}^{n} \frac{e^2}{|r_i - r_j|} - \sum_{I,i} \frac{Z_I e^2}{|R_I - r_i|}, \tag{2.1.3}$$

where the indexes I and J are for nuclei, i and j for electrons, RI and MI are positions and

masses of the nuclei, r_i and m_e of the electrons, Z_I the atomic number of nucleus I. where the first term describes the potential energy of Coulomb interaction between nuclei, the second term is the Coulomb potential energy between electrons and the third term is the Coulomb potential energy between nucleus and electron. The Schrödinger equation for this many body system can be written as,

$$\hat{H}\Psi(\{R_I\}\{r_i\}) = E\Psi(\{R_I\}\{r_i\}), \qquad (2.1.4)$$

where $\Psi(\{R_I\}\{r_i\})$ is the total wavefunction of the system. From quantum mechanics, if the above Schrödinger equation can be solved, many properties of the system are known. However, it is not possible to solve it actually. Born-Oppenheimer (BO) approximation was made by Born and Oppenheimer [48]. It states that since the electrons are much lighter than nuclei, they move much faster than the nuclei. Thus, the movement of nuclei and electrons can be separated. Then, we can consider the nuclei are fixed classically when consider the movement of electrons. Therefore, the original total wavefunction become:

$$\Psi(\{R_I\}\{r_i\}) = \Theta(\{R_I\})\phi(\{r_i\}\{R_I\}), \qquad (2.1.5)$$

where $\Theta(\{R_I\})$ describes the nuclei and $\phi(\{R_I\}\{r_i\})$ describes the electrons. With the BO approximation, Eq. (2.1.4) can be divided into two separate Schrödinger equations [50], which are Schrödinger equation for electrons:

$$\hat{H}_e\phi(\{r_i\}\{R_I\}) = V(\{R_I\})\phi(\{r_i\}\{R_I\}), \qquad (2.1.6)$$

where

$$\hat{H}_e = -\sum_{i}^{n}\frac{\hbar^2}{2m_e}\nabla_{r_i}^2 + \frac{1}{2}\sum_{I=1}^{N}\sum_{\substack{J=1\\J\neq I}}^{N}\frac{Z_I Z_J e^2}{|R_I - R_J|} + \frac{1}{2}\sum_{i=1}^{n}\sum_{\substack{j=1\\j\neq i}}^{n}\frac{e^2}{|r_i - r_j|} - \sum_{I,i}\frac{Z_I e^2}{|R_I - r_i|}, \quad (2.1.7)$$

and Schrödinger equation for nuclei,

$$\left[-\sum_{I}^{N}\frac{\hbar^2}{2M_I}\nabla_{R_I}^2 + V(\{R_I\})\right]\Theta(\{R_I\}) = E'\Theta(\{R_I\}). \qquad (2.1.8)$$

Eq. (2.1.6) is the equation for the electrons with the nuclei positions fixed. The eigenvalue of the energy $V(\{R_I\})$ depends parametrically on the positions of the nuclei. After

solving Eq. (2.1.6), $V(\{R_I\})$ is known and by applying it to Eq. (2.1.8), which has only nuclei degrees of freedom, the motion of the nuclei will be obtained. Eq. (2.1.8) is sometimes replace by a Newton equation, i.e., to move the nuclei classically, using ∇V as the forces. Then the whole problem is solved [50].

The BO approximation is to separate the movement of electrons and nuclei and simplify the Schrödinger equation. Now we can consider that the electrons are moving in a static external potential $V_{ext}(\vec{r})$ formed by the nuclei, which is the starting point of DFT [50]. On the basis of BO approximation, Bohn and Huang extend it into a Born-Huang (BH) approximation [51] to take into account more nonadiabatic effect in the electronic Hamiltonian.

2.1.2 Thomas-Fermi-Dirac Approximation

The Thomas-Fermi (TF) model was proposed by Thomas [52] and Fermi [53] before the developing of DFT. In this model, they used the electron density $n(\vec{r})$ as the basic variable other than the wavefunction. In this model, the exchange and correlation among electrons was neglected. Then, the total energy of a system in an external potential $V_{ext}(\vec{r})$ can be written as a functional of the electron density $n(\vec{r})$ as:

$$E_{TF}[n(\vec{r})] = A_1 \int n(\vec{r})^{5/3}\, d\vec{r} + \int n(\vec{r})\, V_{ext}(\vec{r}) d\vec{r} + \frac{1}{2}\iint \frac{n(\vec{r})n(\vec{r}')}{|\vec{r}-\vec{r}'|} d\vec{r}d\vec{r}'. \quad (2.1.9)$$

where the first term is the kinetic energy of the non-interacting electrons in a homogeneous electron gas (HEG) with $A_1 = \frac{3}{10}(3\pi^2)^{2/3}$ in atomic units ($\hbar = m_e = e = 4\pi/\epsilon_0$). By adding all of the free-electron energy state $\varepsilon_k = k^2/2$ up to the Fermi wavevector $k_F = [3\pi^2 n(\vec{r})]^{1/3}$, the kinetic energy density of a HEG can be obtained as:

$$t_0[n(\vec{r})] = \frac{2}{(2\pi)^3}\int_0^{k_F} \frac{k^2}{2} 4\pi k^2 d\vec{k} = A_1 n(\vec{r})^{5/3}, \qquad (2.1.10)$$

The second term is the classical electrostatic energy of the nucleus-electron Coulomb interaction. The third term is the classical electrostatic Hartree energy approximated by the classical Coulomb repulsion between electrons. In 1930, Dirac [54] adds a local exchange term

$A_2 \int n(\vec{r})^{4/3}\, d\vec{r}$ to the Thomas-Fermi model with $A_2 = -\frac{3}{4}(3/\pi)^{1/3}$, then Eq. (2.1.9) become

$$E_{TFD}[n(\vec{r})] = A_1 \int n(\vec{r})^{5/3}\, d\vec{r} + \int n(\vec{r})\, V_{ext}(\vec{r}) d\vec{r} + \frac{1}{2}\iint \frac{n(\vec{r})n(\vec{r}')}{|\vec{r}-\vec{r}'|} d\vec{r} d\vec{r}' + A_2 \int n(\vec{r})^{4/3}\, d\vec{r}. \quad (2.1.11)$$

The ground state density and energy can be obtained by minimizing the Thomas-Fermi-Dirac equation (2.1.11) subject to the restriction condition of the conservation of the total number of electrons. By using the Lagrange multipliers, we can obtain the solution in the stationary condition:

$$\delta\{E_{TFD}[n(\vec{r})] - \lambda[\int n(\vec{r})\, d\vec{r} - N]\} = 0, \quad (2.1.12)$$

where λ is a constant known as a Lagrange multiplier, whose physical meaning is the chemical potential. Eq. (2.1.12) leads to the Thomas-Fermi-Dirac equation,

$$\frac{5}{3}A_1 n(\vec{r})^{2/3} + V_{ext}(\vec{r}) + \int \frac{n(\vec{r}')}{|\vec{r}-\vec{r}'|} d\vec{r}' + \frac{4}{3}A_2 n(\vec{r})^{1/3} - \lambda = 0. \quad (2.1.13)$$

Although this was an important first step, the Thomas-Fermi equation's accuracy is limited because the resulting expression for the kinetic energy is only approximate, and because the method does not attempt to represent the exchange energy of an atom as a conclusion of the Pauli principle. A term for the exchange energy was added by Dirac. However, the Thomas-Fermi-Dirac theory remained rather inaccurate for most applications. The largest source of error was in the representation of the kinetic energy, followed by the errors in the exchange energy, and due to the complete neglect of electron correlation. Although it is not good enough to describe electrons in matter, its basic concept to use electron density as the variable provides the basis for Density Functional Theory [50].

2.1.3 Hohenberg-Kohn Theorems

Density functional theory is made possible by the existence of two ingeniously simple theorems put forward and proven by Hohenberg and Kohn [35], which are the two Hohenberg-Kohn (HK) Theorems.

The first theorem states that the external potential $V_{ext}(\vec{r})$, and hence the total energy, is a unique functional of the electron density $n(\vec{r})$ [35] (In other words, the ground state particle

density uniquely determines all properties of the system completely). In the following, we will verify this theorem. The only case considered here is that the ground state of the system is non-degenerate. The proof is based on minimum energy principle [50]. Suppose there are two different external potentials $V_{ext}(\vec{r})$ and $V'_{ext}(\vec{r})$ which differ by more than a constant. And we assume that both of them will lead to the same ground state density $n_0(\vec{r})$. Two different Hamiltonians, $\hat{H}$ and $\hat{H}'$, are given by these two external potentials. Both of these two Hamiltonians have the same ground state density $n_0(\vec{r})$ but have different ground state wavefunctions, Ψ and Ψ', with $\hat{H}\Psi = E_0\Psi$ and $\hat{H}'\Psi' = E'_0\Psi'$. Ψ' is not the ground state of $\hat{H}$, so it meet the following inequation,

$$\begin{aligned} E_0 &< \langle\Psi'|\hat{H}|\Psi'\rangle \\ &< \langle\Psi'|\hat{H}'|\Psi'\rangle + \langle\Psi'|\hat{H}-\hat{H}'|\Psi'\rangle \\ &< E'_0 + \int n_0(\vec{r})[V_{ext}(\vec{r}) - V'_{ext}(\vec{r})]\,d\vec{r}\,, \end{aligned} \qquad (2.1.14)$$

similarly,

$$\begin{aligned} E'_0 &< \langle\Psi'|\hat{H}'|\Psi'\rangle \\ &< \langle\Psi'|\hat{H}|\Psi'\rangle + \langle\Psi'|\hat{H}' - \hat{H}|\Psi'\rangle \\ &< E_0 + \int n_0(\vec{r})[V'_{ext}(\vec{r}) - V_{ext}(\vec{r})]\,d\vec{r}\,, \end{aligned} \qquad (2.1.15)$$

If we add these two together, the contradictory inequality are obtained.

$$E_0 + E'_0 < E_0 + E'_0. \qquad (2.1.16)$$

There are no two different external potentials $V_{ext}(\vec{r})$ give rise to the same ground state density $n_0(\vec{r})$, i.e., the ground state density determines the external potential $V_{ext}(\vec{r})$, except for a constant. Therefore, although the exact formula is unknown, it is one one-to-one mapping from the ground state density $n_0(\vec{r})$ to the external potential $V_{ext}(\vec{r})$ [50].

The second theorem states that there exists a universal functional $F[n(\vec{r})]$ of the density, independent of the external potential $V_{ext}(\vec{r})$, such that the global minimum value of the energy functional $E[n(\vec{r})] = \int n(\vec{r})V_{ext}(\vec{r})d\vec{r} + F[n(\vec{r})]$ is the exact ground state energy of the

system and the exact ground state density $n_0(\vec{r})$ minimizes this functional [35]. Thus the exact ground state energy and density are fully determined by the functional $E[n(\vec{r})]$.

In the following, this theorem is proved. The universal functional $F[n(\vec{r})]$ can be expressed as

$$F[n(\vec{r})] \equiv T[n(\vec{r})] + E_{int}[n(\vec{r})], \qquad (2.1.17)$$

where $T[n(\vec{r})]$ is the kinetic energy and $E_{int}[n(\vec{r})]$ is the interaction energy among the particles.

According to variational principle, the energy functional $E[\Psi']$ is

$$E[\Psi'] = \langle \Psi' | \hat{T} + \hat{V}_{int} + \hat{V}_{ext} | \Psi' \rangle , \qquad (2.1.18)$$

It has its global minimum value only when Ψ' equals to the ground state wavefunction Ψ_0, with the restriction conditinon of the conservation of the total number of the particles. According to theorem, Ψ' must correspond to a ground state with particle density $n'(\vec{r})$ and external potential $V'_{ext}(\vec{r})$, then $E[\Psi']$ is a functional of $n'(\vec{r})$.

According to variational principle,

$$\begin{aligned} E[\Psi'] &= \langle \Psi' | \hat{T} + \hat{V}_{int} + \hat{V}_{ext} | \Psi' \rangle \\ &= E[n'(\vec{r})] \\ &= \int n'(\vec{r})\, V'_{ext}(\vec{r}) d\vec{r} + F[n'(\vec{r})] \\ &> E[\Psi_0] \qquad (2.1.19) \\ &= \int n_0(\vec{r})\, V_{ext}(\vec{r}) d\vec{r} + F[n'(\vec{r})] \\ &= E[n_0(\vec{r})]. \end{aligned}$$

Therefore, only when the minimum value of density $n(\vec{r})$, which is $n_0(\vec{r})$, is attained, the energy functional $E[n(\vec{r})] = \int n(\vec{r}) V_{ext}(\vec{r}) d\vec{r} + F[n(\vec{r})]$ will evaluate for the correct ground state density $n_0(\vec{r})$. Thus one would find the exact ground state density and energy by minimizing the total energy functional of the system by variations of the density $n(\vec{r})$ [50].

HK theorems already put charge density $n(\vec{r})$ as the basic variable, but the universal functional $F[n(\vec{r})]$ is needed to obtain to calculate the properties of a system. Next, we will discuss the Kohn-Sham equation proposed by Kohn and Sham [36], which will give the solution

to this problem.

2.1.4 Kohn-Sham Equation

Kohn-Sham (KS) equation [36] successfully puts Hohenberg-Kohn theorems into practical use and makes DFT calculations possible and successfully converts the many body system to one body system. This is the reason that DFT became the most popular tool for electronic structure calculations. Kohn–Sham equation is the Schrödinger like equation of a quasi-particles system of non-interacting electrons that generate the same density as any given system of interacting particles, convert many-body system into one body system. It maps the original interacting system with real potential onto a quasi-particle system whereby the electrons move within an effective potential $V_{eff}(\vec{r})$. For the auxiliary quasi-particle system, the auxiliary Hamiltonian is

$$\hat{H}_{eff} = -\frac{1}{2}\nabla^2 + V_{eff}(\vec{r}) , \qquad (2.1.20)$$

in atomic units $\hbar = m_e = e = \frac{4\pi}{\epsilon_0} = 1$. For a system with N non-interacting electrons, the ground state can be obtained if the N one-electron Schrödinger equations can be solved,

$$[-\frac{1}{2}\nabla^2 + V_{eff}(\vec{r})]\psi_i(\vec{r}) = \varepsilon_i\psi_i(\vec{r}) , \qquad (2.1.21)$$

where only one electron in each of the N orbitals $\psi_i(\vec{r})$ with the lowest eigenvalues ε_i. The density of the non-interacting system can be constructed as:

$$n(\vec{r}) = \sum_{i=1}^{N} |\psi_i(\vec{r})|^2, \qquad (2.1.22)$$

which is subject to the conservation condition:

$$\int n(\vec{r})d\vec{r} = N . \qquad (2.1.23)$$

The non-interacting particle kinetic energy $T_s[n(\vec{r})]$ is given by,

$$T_s[n(\vec{r})] = -\frac{1}{2}\sum_{i=1}^{N} \psi_i^*(\vec{r})\nabla^2\psi_i(\vec{r})d\vec{r} , \qquad (2.1.24)$$

then the universal functional $F[n(\vec{r})]$ become

$$F[n(\vec{r})] = T_s[n(\vec{r})] + E_H[n(\vec{r})] + E_{XC}[n(\vec{r})], \quad (2.1.25)$$

where $E_H[n(\vec{r})]$ is the classic electrostatic (Hartree) energy of the electrons,

$$E_H[n(\vec{r})] = \frac{1}{2}\iint \frac{n(\vec{r})n(\vec{r}')}{|\vec{r}-\vec{r}'|}d\vec{r}d\vec{r}', \quad (2.1.26)$$

and $E_{XC}[n(\vec{r})]$ is the exchange-correlation energy, which includes all many-body effects, such as the difference between the real and non-interacting kinetic energies and the non-classical contribution to the electron-electron interactions, of which the exchange energy is a part. By minimizing the energy functional $E[n(\vec{r})] = \int n(\vec{r})\, V_{ext}(\vec{r})d\vec{r} + F[n(\vec{r})]$, the ground state energy of a many-body system can be obtained.Here, it subjects to the restriction condition of the conservation of the total number of electrons,

$$\delta\left\{F[n(\vec{r})] + \int n(\vec{r})\, V_{ext}(\vec{r})d\vec{r} - \lambda\left[\int n(\vec{r})\, d\vec{r} - N\right]\right\} = 0, \quad (2.1.27)$$

and the resulting equation is

$$\lambda = \frac{\delta F[n(\vec{r})]}{\delta n(\vec{r})} + V_{ext}(\vec{r}) = \frac{\delta T_s[n(\vec{r})]}{\delta n(\vec{r})} + V_{KS}(\vec{r}), \quad (2.1.28)$$

where λ is the chemical potential,

$$\begin{aligned} V_{eff}(\vec{r}) &= V_{ext}(\vec{r}) + V_H(\vec{r}) + V_{XC}(\vec{r}) \\ &= V_{ext}(\vec{r}) + \frac{\delta E_H[n(\vec{r})]}{\delta n(\vec{r})} + \frac{\delta E_{XC}[n(\vec{r})]}{\delta n(\vec{r})}, \end{aligned} \quad (2.1.29)$$

is the KS one-particle potential with the Hartree potential $V_H(\vec{r})$

$$V_H(\vec{r}) = \frac{\delta E_H[n(\vec{r})]}{\delta n(\vec{r})} = \int \frac{n(\vec{r}')}{|\vec{r}-\vec{r}'|}d\vec{r}', \quad (2.1.30)$$

and the XC potential $V_{XC}(\vec{r})$

$$V_{XC}(\vec{r}) = \frac{\delta E_{XC}[n(\vec{r})]}{\delta n(\vec{r})}, \quad (2.1.31)$$

Equations (2.1.21), (2.1.22), (2.1.29) is the main equations of the well-known KS equations, which must be solved self-consistently because $V_{eff}(\vec{r})$ depends on the charge density through the XC potential while the charge density is constructed by the N

wavefunctions. The XC energy is needed to obtain the wavefunction. Usually, the starting point of the self-consistency loop is to guess an input charge density to start.

The XC energy functional $E_{XC}[n(\vec{r})]$ in effective potential is unknown, which will lead that the KS theory is approximate. $E_{XC}[n(\vec{r})]$ can be expressed as

$$E_{XC}[n(\vec{r})] = T[n(\vec{r})] - T_S[n(\vec{r})] + E_{int}[n(\vec{r})] - E_H[n(\vec{r})], \quad (2.1.32)$$

where $T[n(\vec{r})]$ and $E_{int}[n(\vec{r})]$ are the exact kinetic and interaction energies between the electrons of the many-body system, respectively. In order to obtain a good description of a realistic many-body system, some approximations are used get a more accurate XC potential. The most widely used approximations are the local density approximation (LDA) and the generalized-gradient approximation (GGA).

2.1.5 Local Density Approximation

The density functional theory as it has been discussed up to this point is exact and no approximation has been introduced into this theory. However, the exchange correlation energy functional $E_{XC}[n(\vec{r})]$ is still unknown which leads the KS equations unsolvable. Although the exact XC energy functional $E_{XC}[n(\vec{r})]$ is very complicated, simple but successful approximations to it have been made. These approximations not only predict many properties of many-body systems well but also reduce computational costs to some extent, leading to the wide use of DFT for electronic structure calculations. The local density approximation (LDA) is the most widely used approximation. In this approximation, the XC energy per electron at a point $\vec{r}$ is considered the same as that for a homogeneous electron gas (HEG) that has the same electron density at the point $\vec{r}$. The total exchange-correlation functional $E_{XC}[n(\vec{r})]$ can be written as,

$$\begin{aligned} E_{XC}^{LDA}[n(\vec{r})] &= \int n(\vec{r})\varepsilon_{XC}^{H}(n(\vec{r}))d\vec{r} \\ &= \int n(\vec{r})[\varepsilon_X^H(n(\vec{r})) + \varepsilon_C^H(n(\vec{r}))]\, d\vec{r} \quad (2.1.33) \\ &= E_X^{LDA}[n(\vec{r})] + E_C^{LDA}[n(\vec{r})], \end{aligned}$$

for spin unpolarized systems and

$$E_{XC}^{LDA}[n_{\uparrow}(\vec{r}), n_{\downarrow}(\vec{r})] = \int n(\vec{r})\varepsilon_{XC}^{H}\left(n_{\uparrow}(\vec{r}), n_{\downarrow}(\vec{r})\right)d\vec{r}, \qquad (2.1.34)$$

for spin polarized systems [56], where the XC energy density $\varepsilon_{XC}^{H}(n(\vec{r}))$ is a function of the charge density, and can be decomposed into exchange energy density $\varepsilon_{X}^{H}(n(\vec{r}))$ and correlation energy density $\varepsilon_{C}^{H}(n(\vec{r}))$ so that the XC energy functional can be decomposed into exchange energy functional $E_{X}^{LDA}[n(\vec{r})]$ and correlation energy functional $E_{C}^{LDA}[n(\vec{r})]$ linearly [50]. By using the expression for a HEG, the exchange energy functional $E_{X}^{LDA}[n(\vec{r})]$ can be expressed as the following [54],

$$E_{X}^{LDA}[n(\vec{r})] = \int n(\vec{r})\varepsilon_{X}^{H}\left(n(\vec{r})\right)d\vec{r}$$

$$= -\frac{3}{4}\left(\frac{3}{\pi}\right)^{\frac{1}{3}}\int\left(n(\vec{r})\right)^{\frac{4}{3}}d\vec{r}\,, \qquad (2.1.35)$$

where $\epsilon_{X}^{H}\left(n(\vec{r})\right) = -\frac{3}{4}\left(\frac{3}{\pi}\right)^{\frac{1}{3}}\left(n(\vec{r})\right)^{\frac{1}{3}}$ (2.1.36) is the exchange energy density of the unpolarized HEG introduced first by Dirac [54]. The correlation energy of the HEG cannot be expressed analytically, only the correlation energy in the high and low density limits corresponding to infinitely weak and infinitely strong correlations can be expressed. The correlation energy density of the HEG at high density limit can be expressed as,

$$\varepsilon_{C}^{H} = A\cdot\ln(r_s) + B + r_s[C\cdot\ln(r_s) + D]\,, \qquad (2.1.37)$$

and the low density limit can be expressed as

$$\varepsilon_{C}^{H} = \frac{1}{2}\left(\frac{g_0}{r_s} + \frac{g_1}{r_s^{3/2}} + \cdots\right), \qquad (2.1.38)$$

where the Wigner-Seitz radius r_s is related to the density as

$$\frac{4}{3}\pi r_s^3 = \frac{1}{n}. \qquad (2.1.39)$$

To obtain the correlation energy density at intermediate density accurately, quantum Monte Carlo (QMC) simulations for the energy of the HEG is used and have been performed at several intermediate density values [57]. Most local density approximations to the correlation energy density interpolate these accurate values from QMC simulations while reproducing the

exactly known limiting behavior. Depending on the analytic forms used for ε_C^H, different local density approximations were proposed including Vosko-Wilk-Nusair [58], Perdew-Zunger [59], Cole-Perdew [60] and Perdew-Wang [61].

In LDA, the inhomogeneities in the electronic density are ignored. However, as a simple correction to the exchange-correlation energy, LDA is surprisingly successful and even works reasonably well in systems where the electron density is rapidly varying. This is because that LDA gives the correct sum rule to the exchange-correlation hole. For LDA, a total electronic charge of one electron was excluded from the neighborhood of the electron at r. On the other hand, it tends to underestimate atomic ground state energies and ionization energies, while overestimating binding energies. Especially, it makes large errors in predicting the energy gaps of semiconductors. Due to the limitation of LDA, some new approximations of the XC energy functional beyond the LDA have been developed through the addition of density gradient corrections to incorporate longer range gradient effects.

2.1.6 Generalized Gradient Approximation

The real charge density, which is inhomogeneous, could be very different from the HEG. The XC energy of inhomogeneous charge density can be significantly different from the HEG result. To overcome this problem of LDA, generalized-gradient approximations (GGA), which is an approximation beyond LDA, has been developed, in which the XC energy is improved by introducing density gradient corrections and higher spatial derivatives of the electron density. In many cases, GGA gives better results than LDA. There are three most widely used GGAs, which are proposed by Becke (B88) [62], Perdew et al. [63], and Perdew, Burke and Enzerhof (PBE) [64].

Based on the general form of Eq. (2.1.33), the XC energy functional of GGA can be defined as Eq. (2.1.41), which include corrections of density gradient $\nabla n(\vec{r})$

$$E_{XC}^{GGA}[n_\uparrow(\vec{r}), n_\downarrow(\vec{r})] = \int n(\vec{r})\varepsilon_{XC}^H(n_\uparrow(\vec{r}), n_\downarrow(\vec{r}), \nabla n_\uparrow(\vec{r}), \nabla n_\downarrow(\vec{r}), \dots)d\vec{r}$$
$$= \int n(\vec{r})\varepsilon_X^H\big(n(\vec{r})\big)\, F_{XC}(n_\uparrow(\vec{r}), n_\downarrow(\vec{r}), \nabla n_\uparrow(\vec{r}), \nabla n_\downarrow(\vec{r}), \dots)d\vec{r}, \quad (2.1.41)$$

where F_{XC} is dimensionless and $\varepsilon_X^H(n(\vec{r}))$ is the exchange energy density of the unpolarized HEG. F_{XC} can be decomposed linearly into exchange contribution F_X and correlation contribution F_C as $F_{XC} = F_X + F_C$. In predicting bond length and binding energy of molecules, crystal lattice constants, GGA generally make an improvement on LDA. Especially when the charge density varies rapidly, GGA is applied. Nevertheless, GGA sometimes overcorrects LDA results in ionic crystals where LDA fit well. Therefore, GGA will overestimate it. However, for materials where the electrons tend to be localized and strongly correlated such as transition metal oxides, both LDA and GGA perform badly, such as also underestimating the band gap. The problem is that no systematic way has been developed to improve the functionals for exchange and correlation energy [50].

2.1.7 Hybrid Functional

Due to the drawbacks of LDA and GGA, a number of beyond them have been developed in the past few years and are being incorporated [65]. Hybrid density functionals [66], which incorporate exact exchange by combining Hartree-Fock, have further improved the LDA and GGA results. Correlation energy is still processed by GGA. Hybrid functionals are the only fully nonlocal functionals in the density and orbitals. Hyde, Scuseria and Ernzerhof [42, 71-72] provided a new hybrid functional, which is called HSE and applies a screened Coulomb potential to the exchange interaction in order to screen the long-range part of the HF exchange:

$$E_{XC}^{HSE} = aE_X^{HF,SR} + (1-a)E_X^{PBE,SR} + E_X^{PBE,LR} + E_C^{PBE}, \qquad (2.1.42)$$

where $E_X^{HF,SR}$ is the short-range Hartree-Fock exchange, $E_X^{PBE,SR}$ and $E_X^{PBE,LR}$ are the short-range and long-range components of PBE exchange, and a is the Hartree-Fock mixing parameter ($a = 0.25$ is the default value in VASP). The short-range and long-range parts are determined by splitting the Coulomb operator into short-range and long-range parts:

$$\frac{1}{r} = \frac{\mathrm{erfc}(\omega r)}{r} + \frac{\mathrm{erf}(\omega r)}{r}, \qquad (2.1.43)$$

where the first term is short-range and the second term is long range. The complementary error

function is $\mathrm{erfc}(\omega r) = 1 - \mathrm{erf}\,(\omega r)$ and ω is an adjustable parameter. erf is the error function and erfc is the complementary error function, separately. And $\omega = 0.15 a_0^{-1}$ [42] is the default screening parameter based on molecular basis tests. In our research, the HSE hybrid functional is used.

2.2 Plane Wave Basis Sets and Pseudopotential Approximation

Solving the Kohn-Sham equations is an integral-differential problem, which is difficult to achieve in practical calculations. Therefore, it is necessary to transform this into an easier one. This can be achieved by expanding the electronic wavefunctions with a basis set and by using pseudopotential approximation.

2.2.1 Plane Wave Basis Sets

The popular basis sets include plane waves, real space grids, and atomic orbitals. We need to choose a basis set to expand the wavefunctions $\Psi_i(\vec{r})$. Choosing a basis set is a very important task. This is because that the basis set will affect how much memory will be required to store the wavefunctions and Hamiltonian, and how much run-time will be required to solve for the eigenstates. Moreover, the completeness of the basis set will also influence the accuracy of the results. Given the importance of the basis set, it is crucial that it be chosen to meet the desired speed, accuracy and memory constraints [125]. It usually balances the accuracy and the computational cost. Among all the basis sets, plane wave basis set [73] has become a very popular basis set. It is discussed in the following.

Naturally, plane wave has been used as a basis set for a periodic system, which was described by Bloch's theorem. According the Bloch's theorem, the electronic wavefunction can be written as [74]

$$\psi_{i\vec{k}}(\vec{r}) = e^{i\vec{k}\vec{r}} u_i(\vec{r}), \qquad (2.2.1)$$

where $u_i(\vec{r})$ is a cell periodic function, and $\vec{k}$ is the Bloch wavevector. Since $u_i(\vec{r})$ is a periodic function, it can be expanded into a discrete sum of plane waves

$$u_i(\vec{r}) = \sum_{\vec{G}} c_{i\vec{G}}\, e^{i\vec{G}\vec{r}}, \qquad (2.2.2)$$

where $\vec{G}$ are the reciprocal lattice vectors, and $c_{i\vec{G}}$ are the expansion coefficients. In practice, at an upper cutoff for $\vec{G}$, the sum will be terminated, so that expansion becomes finite. Meanwhile, the wavefunctions still can be well represented with certain accuracy. By using the above expression for $u_i(\vec{r})$, the wavefunction can be represented as a plane wave sum

$$\psi_{i\vec{k}} = \sum_{\vec{G}} c_{i,\vec{k}+\vec{G}}\, \vec{G} e^{i(\vec{k}+\vec{G})\vec{r}}, \qquad (2.2.3)$$

in which $c_{i,\vec{k}+\vec{G}}$ are Fourier transform coefficients.

Some reasons make plane wave basis set [73] become a very popular basis set. Firstly, analytic expressions can be easily derived, and programmed from plane wave basis set. This is because that the matrix elements in the plane wave basis set are Fourier transforms, which can be evaluated by using a canned Fast Fourier Transform routine. Secondly, the completeness of plane wave basis set in turn implies that the wavefunctions will have certain accuracy and the eigenvalues and total energy will be also accurate. On the other hand, plane wave basis set also has some major disadvantages. First, to expand the wavefunctions, many plane waves are needed. Therefore, the large memory is required and it will take a long runtime to finish the job. When the elements have partially filled d orbitals, it will need even large amount of plane wave basis set. This is because d orbitals are very sharp and not easily to expand. Therefore, unlike s orbitals, d orbitals need more plane waves expand them accurately. Secondly, by using plane wave basis set, an assumption was made that the system is periodic in all directions. For a surface or a molecule, plane wave basis set is not a natural choice. However, this problem can be solved by creating a supercell, and put the molecule in the center of supercell to avoid the interaction between them. This method itself will increase the number of plane wave to expand the wavefunctino by increasing the size of the supercell [125]. The larger the size of the supercell is, the more plane waves will be needed.

In summary, plane wave plane have both advantages and disadvantages. Although it is complete and accurate to work for periodical systems, plane waves require a large amount of memory and run-time.

2.2.2 Pseudopotential Approximation

Density functional theory provides a theoretical basis on how to solve the many-body system in an external potential $V_{ext}(\vec{r})$. For a case of one an atom, the external potential energy can be $-\frac{Z_I e^2}{r}$, where $Z_I e$ is the charge of the nucleus, and r is the distance from the nucleus. By using this potential energy, the Kohn-Sham single particle eigenstates ψ_i for all the electrons in the system can be calculated, including both of the core and valence electrons. However, the core electrons have very little influence on most physical properties of materials, especially on the properties of the band gap. Therefore, the core electrons are usually treated with nuclei together while the valence electrons are treated separately. This separation will save some memory. The above is the theoretical basis of the pseudopotential approximation [75-76], in which the core electrons are combined with nuclei together and a weaker ionic pseudopotential V_{pseudo} is introduced to substitute the the $-\frac{Z_I e^2}{r}$ potential. The pseudopotential include the effect comes from both of nuclei and the core electrons. Therefore, when the radius is beyound cutoff radius r_{cut}, the pseudopotential is merely given by $-\frac{Z_I e^2}{r}$, where $Z_I e$ is the net charge of the ionic core. Figure 2.1 shows the comparison between a pseudopotential and $-\frac{Z_I e^2}{r}$ potential in conjunction with their corresponding valence wavefunctions. From Figure 2.1, we can see that, unlike the all-electron orbital, the pseudopotential does not diverge at the origin and the pseudo-atomic orbital does not oscillate in the core region. Therefore, much less plane waves are needed to expand it [125].

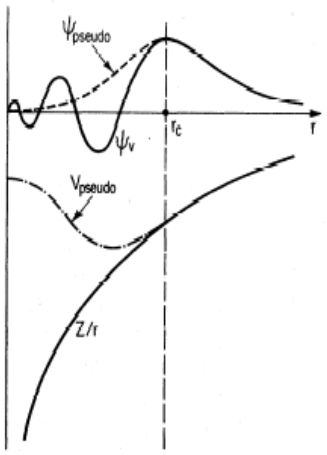

Figure 2.1 Comparison between pseudopotential and real potential

Before the construction of pseudopotentials, a restriction condition is needed to be set that physical properties of the atom remain invariant. Then, simplify the spatial variation of the pseudo orbital. In particular, the same valence eigenvalues as the all-electron calculation must be yielded by a pseudopotential calculation. In addition, the potential is also chosen to make sure that the corresponding pseudo orbitals do not oscillate in the core region. And the pseudo orbitals is needed to match the all-electron orbitals beyond the cutoff radius r_{cut}. To meet the second requirement, we must add some restriction condition that the pseudopotential matches the true potential beyond the cutoff radius r_{cut}. Last, norm-conservation is another common requirement, which means that the pseudo charge inside the core region matches the true charge. In general, most pseudopotentials are non-local, which means that they are not simply a function of position [125]. A popular non-local, norm-conserving pseudopotential is given by the construction procedure of Hamman-Schlüter-Chiang [77], for which

$$V_{pseudo} = V_l(\vec{r}) + V_{nl}\,, \qquad (2.2.4)$$

where $V_l(\vec{r})$ is a local term that depends only on r and equals to the ionic potential $-\frac{Z_I e^2}{r}$ beyond the cutoff radius r_{cut}. In addition, V_{nl} is the non-local term that can be written as

$$V_{nl} = \sum_{l=0}^{2} V_l(\vec{r})\hat{P}_l\,, \qquad (2.2.5)$$

where $\hat{P}_l$ is the projector onto angular momentum l, and $V_l(\vec{r})$ are angular momentum dependent, short-ranged potentials that vanish beyond the pseudopotential cutoff r_{cut}.

Although pseudopotentials are much more complicated compared to the true $-\frac{Ze^2}{r}$ potential, they have such advantage that taking short computational time and saving memory. When pseudopotential is used, all of the core electrons are no longer included in a calculation. Therefore, their corresponding wavefunction will not been calculated. This will save a lot of computational power since only valance electrons are included in the calculation. The number of valence electrons is much samller than the total number of electrons. Moreover, pseudopotentials over the all-electron potential have another advantage that the pseudo wavefunctions do not oscillate in the core region, which implies that the wavefunctions can be easily expanded numerically by fewer plane waves. These two advantages make the pseudopotentials become the mostly common used in many first principles calculations, in spite of their complicated non-local formulations [125].

Afterward, Projective Augmented Wave [95] has been developed. This approach combines the formal simplicity of the traditional plane wave pseudopotential approach and the versatility of the linear augmented plane wave method [112]. In this approach, it provides the full wave functions which are not accessible with the pseudopotential approach, and the potential is determined from the full charge densities. The accuracy of this method compares well with other existing electronic structure methods.

2.2.3 Solution of Kohn-Sham Equation

The KS equations use non-interacting particle (quasi particles) methods, which give an approach to obtain the exact density and energy of the ground state of a complicated many body system. The effective potential, wavefunctions and the charge density $n(\vec{r})$ closely depend on each other. To calculate the charge density, the wavefunctions are needed. To get the wavefunction of system, the effective potential is needed. To get the effective potential, the charge density is needed. Here, a self consistency method is used to get the solution. The

matrix diagonalization and minimization are the most widely used methods for the KS equations. Conventional matrix diagonalization finds all N_b eigenvectors of a $N_b \times N_b$ matrix, where the computation time scales as N_b^3. This method is usually used for small basis sets, such as a minimal atomic orbital set. But for large basis like plane waves, which is preferably used to expand the wavefunction, matrix diagonalization would be very slow and cost large memory to do it. Therefore, for plane waves, minimization is used. This is because minimization method has such advantage that this method for solving eigenvalue problems can selectively calculate the first m eigenvectors, where in our case $m = N_e/2$ and N_e is the number of electrons. Compared with diagonalization, the runtime for minimization scales will be reduced to only a fraction of the N_b^3 diagonalization scaling. If we want to find the first m eigenvectors, then the runtime for the minimization approach scales as mN_b^2 [125]. However, if all the eigenvectors $(m = N_b)$ are needed to fine, there is no difference in the runtime scaling between these two methods. Therefore, a conclusion can be obtained that the minimization is more efficient because that it does not calculate the wavefunctions which are not needed to perform the simulation, only eigenstates needed is calculated by minimization. However, for diagonalization, it is not this case.

Here, we need mention another important factor is that the Hamiltonian depends on the charge density. In the effective potential, both of Hartree potential and XC potential depends on the charge density. Therefore, to solve the Schrödinger equation, the charge density is required. however, the charge density in turn depends on the wavefunctions. Strictly speaking, the dependence of the Hamiltonian on the eigenstates requires that the eigenvalue problem be solved self-consistently. In other words, the density used to find the Hamiltonian must be the same as the density given by the calculated eigenstates.

To attain self-consistency, an iterative approach must be used. This self-consistent iteration is shown in Figure 2.2.

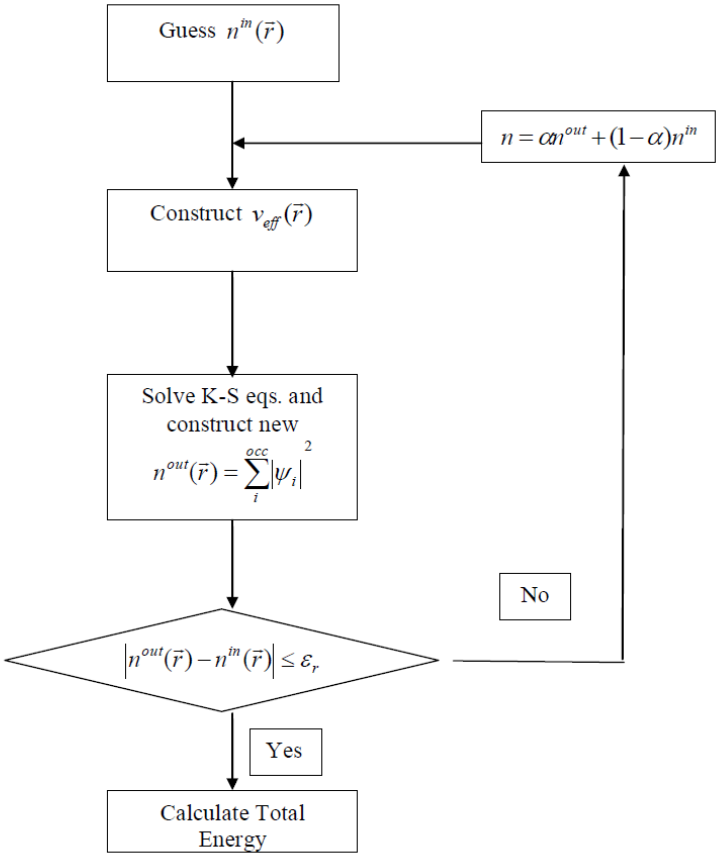

Figure 2.2 Self-consistent calculation flow chart.

The procedure begins by choosing a trial input charge density $n(\vec{r})$. Then the effective potential corresponding to this input density can be found. Using $V_{eff}(\vec{r})$ the Hamiltonian matrix is calculated in the given basis, and then the eigenvectors are found by using matrix diagonalization. These eigenvectors are then used to calculate the wavefunctions, which in turn generate the output density $n(\vec{r})$. In general, the output and input density will not be consistent, and hence the above procedure must be repeated until the solution is self-consistent. In practice the new input density is usually taken to be a linear combination of the output and input densities, since this would speed up convergence. Finally, when the output and input densities are equal, the cycle terminates. After the self-consistency is reached, various quantities can be

calculated including total energy, forces, stress, eigenvalues, electron density of states, and band structure.

2.3 Formation Energy of Defect

The formation energy is the difference in the total crystal energy before and after the defect arises. Usually, an introduced defect causes some lattice distortion and leads to the increase in entropy. Therefore, the formation energy of defect is a positive. The formation energy of a neutral defect [78] can be calculated from

$$\Delta H^{f}(D,0) = E(D,0) - E(P) + \sum_{i}(n_i\,\mu_i^0 + n_i\Delta\mu_i), \qquad (2.3.1)$$

where $E(P)$ is the total energy of the stoichiometric perfect supercell and $E(D,0)$ is the total energy of the super cell with defect. Calculations on the constituent elements of the material in their standard states, in vacuum conditions O_2 and Cu metal, give the elemental energies, μ_i^0, with n being +1 or -1 if an atom is added to or removed from an external reservoir. Varying the chemical potentials, μ_i of each species varies according to the specific equilibrium growth conditions, within the global constraint of the calculated enthalpy of the host; in this instance Cu_2O. For example, there are two limit growth conditions in a vacuum-based environment, which can be Cu rich or O rich. Under Cu-rich/O-poor conditions, Cu is assumed to be in a thermodynamic equilibrium with bulk Cu and, therefore, $\Delta\mu_{Cu} = 0$, then, $\mu_{Cu} = \mu_{Cu}^0$. Then, μ_O can be calculated by μ_{Cu}.

The formation energy of a charged defect can be calculated from

$$\Delta H^{f}(D,q) = \Delta H^{f}(D,0) + q[E_{VBM} + \varepsilon_F + \Delta v(D)], \qquad (2.3.2)$$

where E_{VBM} is the energy of the valence band maximum (VBM) and ε_F is the Fermi level of electrons measured from the VBM. E_{VBM} is energy level of minimum of valence band. $\Delta v(D)$ aligns the VBM of the defective and perfect supercells. Because the perfect supercell cannot be directly applied to the supercell with defect, this alignment correction will improve the accuracy. Also, this is due to the long range nature of the periodic boundary conditions of the supercell

approach [78] and Coulomb potential. A O 1s core level in the supercell which is furthest away from the defect and the core level in the perfect supercell are compared, and the difference between them are used to make the shift to make these two core level are in the same energy level [79], which is given by

$$\Delta v(D) = \varepsilon_{core,1s}(D, q) - \varepsilon_{core,1s}(P), \qquad (2.3.3)$$

where $\varepsilon_{core,1s}(D, q)$ is the O 1s core level of the O atom which is furthest away from the defect location, and $\varepsilon_{core,1s}(P)$ is the O 1s core energy level of the perfect supercell.

In the figure of formation energy, a transition level between different charge states is shown, which means an energy level at which the charge states q_1 and q_2 have equal total energy. This level also can be specified as the thermodynamic ionization level of a given defect, $\varepsilon_D(q_1/q_2)$. We can calculate the transition level by

$$\varepsilon_D(q_1/q_2) = \frac{\Delta H^f(D, q_1) - \Delta H^f(D, q_2)}{q_2 - q_1}, \qquad (2.3.4)$$

and can be directly compared to the trap levels reported in experiments where the final charge state can relax to its equilibrium configuration after the transition [79, 80].

CHAPTER 3

UNDOPED CUPROUS OXIDE

3.1 Introduction

Cuprous oxide (Cu_2O) has been extensively studied as one of the promising solar cell materials [81]. This is due to its direct band gap of 2.1 eV, which is within the appropriate range for photovoltaic cell conversion. Also, it is non-toxicity and the natural abundance of the source materials. Therefore, it is an inexpensive and available semiconductor for solar cell. However, the best reported conversion efficiency from experiments is only 2% [20].

There are three important techniques for preparation of Cu_2O thin film, which include thermal oxidation, sputtering and electrochemical deposition.

Thermal oxidation [83-84] is the most widely used method to produce Cu_2O solar cell. The procedure involves the oxidation of high purity copper in a tube furnace with pure oxygen gas or mixture gas of oxygen and argon at an elevated temperature (1000–1,500℃) for 72Hrs to oxidize the entire Cu_2O. During the process of oxidation, Cu_2O is formed first and after a sufficiently long oxidation time, CuO is formed. This follows the reaction equation below [85]. The unwanted CuO can be removed using an etching solution containing FeCl3, HCl and NaCl [85]. In 1982, Olsen et al. [21] fabricated p-type Cu_2O successfully by thermal oxidation, which lead to only p-type Cu_2O.

$$4\mathrm{Cu} + \mathrm{O}_2 \rightarrow 2\mathrm{Cu}_2\mathrm{O} \qquad (3.1.1)$$

$$2\mathrm{Cu}_2\mathrm{O} + \mathrm{O}_2 \rightarrow 4\mathrm{CuO} \qquad (3.1.2)$$

Reactive sputtering [86] is another method used in the production of Cu_2O. This experiment is also conducted in vacuum condition. A chemical reaction that occurs with the cathode material (Cu in this case) by the active gas (oxygen) either added to the working gas or as the working gas itself. The resistivity of the deposited Cu_2O film can be controlled over a

wide range by simply varying the oxygen pressure.

In both of the above two methods, no n-type Cu_2O was produced. Cu_2O has been known as a naturally p-type semiconductor for a long time [87-90]. However, the n-type Cu_2O is a requirement for the production of Cu_2O homojunction, which has high efficiency than heterojunction. Researchers are trying different ways to fabricate n-type Cu_2O. They found that under specific circumstances, n-type Cu_2O has been deposited electrochemically without any external dopant [22-23, 91]. In 1986, Siripala et al. [22] reported that n-type Cu_2O films were cathodically deposited on metal substrates using a solution of $CuSO_4$. In 2008, Wang et al. [23] successfully fabricated Cu_2O p-n homojunctions by a two-step sequential electrochemical deposition process. The following reaction occurs in the experiments [91]:

$$Cu^{2+} + e^{-} \rightarrow Cu^{+} \qquad (3.1.3)$$

$$2Cu^{+} + 2OH^{-} \rightarrow Cu_2O \downarrow + H_2O \qquad (3.1.4)$$

The experiments conducted by electrochemical deposition make the p-n homojunction possible to further improve the efficiency of Cu_2O solar cell.

Also, in the theoretical part, the first principles methods are used to simulate Cu_2O to prove the existence of n-type Cu_2O. Scanlon [92] and Raebiger [93] reports that n-type Cu_2O does not exist. However, the condition considered in their paper is only vacuum-based growth condition, which is the condition for thermal oxidation and sputtering. On the other side, Wang et al. [24] successfully explained by using LDA that both n-type and p-type can be obtained in different pH values, in which the solution condition is considered.

Also, in the theoretical part, the first principles methods are used to study Cu_2O. Nolan et al. [106] studied Cu_2O by GGA and GGA+U and reported that the delocalized holes around the copper vacancy site will lead to p-type conduction properties. The band gap obtained by GGA is only 0.5eV. Raebiger et al. [93] have shown from GGA+U calculations that Cu_2O is intrinsically p-type, in which V_{Cu} acts as a shallow and efficient hole producer. The band gap obtained in their calculation is 0.43 eV. Scanlon et al. [104] successfully calculated a more exact

value of band gap, which is 2.1eV, by hybrid density functional with 27.5% of Hartree-Fock exchange potential. They also investigated the formation of native defects in Cu_2O giving rise to single-particle levels that are deep in the band gap, consistent with experimentally observed activated, polaronic conduction. All of these three first-principles studies obtained only p-type conductivity in undoped Cu_2O grown form vacuum-based conditions. Later, Wang et al. studied by LDA that the formation of native point defects in cuprous oxide synthesized from solution and different types of conductivity in different solution with different pH values. Both n-type and p-type Cu_2O are obtained in his calculation.

In our research, HSE hybrid density functional [41-42] is used to study the electronic properties and formation energy of Cu_2O, in which a more accurate band gap is obtained and formation of CuO is also considered.

3.2 Crystal Structure

Cu_2O crystallizes in a cubic structure with a lattice constant of 4.27 Å. It is formed by an fcc array of Cu and a bcc array of O atoms. As shown in Figure 3.1, there are 4 Cu atoms and 2 O atoms. Each Cu atom is connected by 2 O atoms. And each O atom is surrounded by a tetrahedron of Cu atoms. This low coordination numbers are very unusual for metal oxides, whose space group belongs to $\mathrm{Pn\bar{3}m}$, which includes the point group with full octahedral symmetry. Only Ag_2O and Pb_2O have this kind of structure [94].

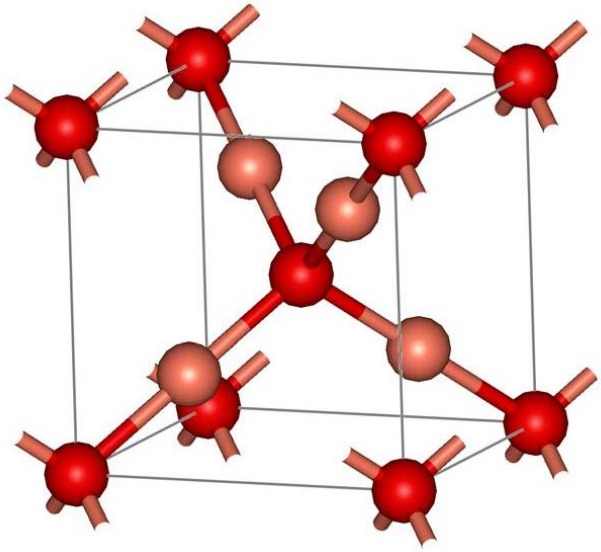

Figure 3.1 Crystal structure of Cu_2O. Deep red balls represent oxygen atoms, while pink ones copper atoms.

3.3 Computational details

All the present calculations were performed using the VASP package [37-41] based on the Kohn-Sham formulism of density-functional theory (DFT). The Generalized Gradient Approximation (GGA) for the exchange correlation functional of Perdew-Burke-Ernzerhof (PBE) [64] was adopted initially. In order to reduce the number of plane wave basis functions necessary for accurately describing the electronic wave functions, the projector augmented wave (PAW) method [95] was used to describe the electron-ion interactions. The PAW potential for Cu was generated from the atomic configuration of $[Ar]3d^{10}4s^{1}$. For O, the atomic configuration to generate the PAW potential was $[He]2s^{2}2p^{4}$. The geometry optimization after an impurity introduced in Cu_2O is conducted using DFT-GGA calculations. But the total energy and the final electronic structure calculations are conducted using the nonlocal screened Heyd-Scuseria-Ernzerhof (HSE) hybrid density functionals [41-42] approach. In the hybrid functional, the exchange part is a mixing of that of PBE and Hartree-Fock (HF), while the correlation part is still that of PBE. In the functional used in the present work, 25% HF and 0.2 Å-1 screening parameter is taken, which is the default setting value in VASP.

3.4 Structural and Electronic Properties

The geometry optimization of Cu_2O is conducted by using GGA-PBE calculations [64]. The calculated crystal lattice constant is 4.32 Å, and the calculated distance of Cu-O bond is 1.87 Å. As Table 3.1 listed, our results are in good agreement with previous results and with known experimental values (The relative error is less than 2%). Also, this demonstrated the PAW potential and GGA-PBE method are reliable in the study of structural properties of Cu_2O and doped Cu_2O.

Table 3.1 Comparison of the lattice constant (a), Cu–O bond lengths, and fundamental band gaps of bulk Cu_2O from previous theoretical and experimental studies and those from the current GGA and GGA+U calculations. Bond distances and lattice parameters are given in Å and Eg is measured in eV.

	a (Å)	Cu-O (Å)	Eg (eV)
LDA[96]	4.18	…..	…..
GGA-PBE[97]	4.29	1.86	0.47
GGA-PBE[126]	4.32	1.87	0.47
GGA-PBE+U[98]	4.28	1.85	0.67
HSE[126]	…..	…..	1.91
HSE[99]	…..	…..	2.12
Expt.[100]	4.27	1.85	2.17

Using the optimized structural parameters for the perfect crystal, the final electronic structure calculations are conducted using both GGA-PBE and HSE hybrid density functionals [41-42]. The band gap obtained from GGA-PBE agrees with other theoretical results. GGA have been used for several decades but usually underestimates the band gap. In our studies, the band gap obtained from HSE is 1.91 eV, which is close to the experimental value. In reference [99], 27.5% is taken so that a larger band gap is obtained. From these results, they verify that electronic structure in semiconductors, especially the band gap, cannot be describe properly by

using GGA. HSE hybrid functional gives a significant improvement on the calculation of band gap.

From the band structure and density of states (DOS), we can see the band gap more clearly. The band structure of Cu_2O is drawn in Figure 3.2, which is obtained from GGA calculation. As it shows, Cu_2O has a direct band gap. However, the band gap is only 0.47 eV.

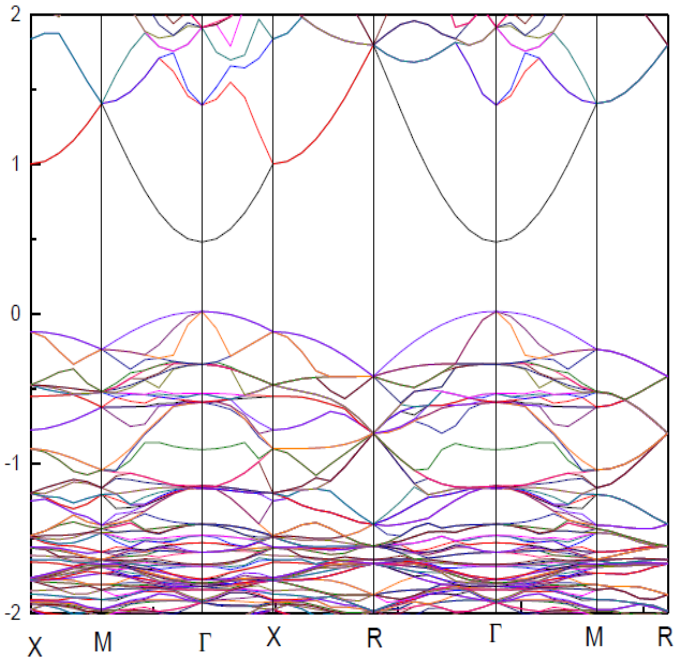

Figure 3.2 Electronic band structure of native Cu_2O. The energy level of valence band maximum corresponds to the zero energy.

In Figure 3.3, the DOS from GGA and HSE are drawn to show the difference of band gap more clearly. From the figure of DOS, we can see that the band gap of Cu_2O based on the GGA is only 0.47 eV, which is consistent with that of the band structure in Figure 3.2. In HSE, the band gap is given a rigid shift, which means that the VBM moves down while CBM moves up. The band gap from hybrid functional is 1.91 eV, which is in good agreement with the experimental value of 2.1 eV. Except the band gap, other structure of DOS is the same between GGA and HSE. They have the same peaks and same shape, which mean that HSE is reliable

to describe the density of states and band gap. However, the HSE calculation is very costly. Therefore, only GGA is used to optimize the structure of Cu_2O to calculate the band structure.

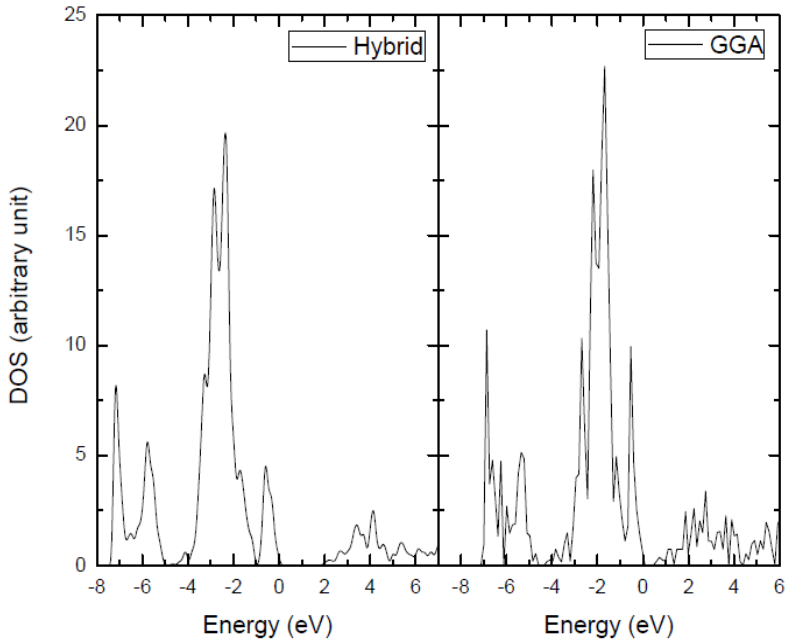

Figure 3.3 Density of state of Cu_2O by Hybrid functional (left) and GGA (right)

3.5 Formation Energies of Native Point Defects

In undoped Cu_2O, the native defects provide the conductivity and determine the type of conduction. There are mainly three different types of native point defects, which are vacancies of Cu or O atom (V_{Cu} and V_O), antisite defects (Cu_O or O_{Cu}), and isolated interstitials (I_O or I_{Cu}). A vacancy was introduced by removing a Cu atom or O atom from its site in the supercell. For the antisite defects, an O atom was replaced by a Cu atom or a Cu atom was substituted by an O atom in the supercell. In the case of isolated interstitials, an atom of Cu or O was put into possible high-symmetry interstitial sites in the supercell. There are three types of interstitial sites with high symmetry. They include two sites with a tetrahedral local symmetry, one at the face-center of the cubic unit-cell (T1) and one in the middle of the side of the cubic (T2), and one site with an octahedral local symmetry (O).

3.5.1 Formation Energies in Vacuum Conditions

From Eq. (2.3.1) in the previous chapter, the total energy of perfect and defect crystal and all chemical potentials are needed to calculate the formation energy. In this case, the formula of formation energy becomes

$$\Delta H^f(D,0) = E(D,0) - E(P) + n_1(\mu^0_{Cu} + \Delta\mu_{Cu}) + n_2(\mu^0_O + \Delta\mu_O) + q(E_{VBM} + E_F), \quad (3.5.1)$$

where μ^0_{Cu} is the chemical potential of Cu in metal Cu, and μ^0_O is the chemical potential of O in O_2 gas. $\mu^0_{Cu} + \Delta\mu_{Cu}$ is the chemical potential of Cu in the current material. The same is for O. In this equation, q can be 0 or +1, -1. For V_{Cu}, $n_1 = 1, n_2 = 0$, and for V_O, $n_1 = 0, n_2 = 1$. So, the formula of formation energy becomes

$$\Delta H^f(V_{Cu},0) = E(V_{Cu},0) - E(P) + \mu^0_{Cu} + \Delta\mu_{Cu} + q(E_{VBM} + E_F), \quad (3.5.2)$$

$$\Delta H^f(V_O,0) = E(V_O,0) - E(P) + \mu^0_O + \Delta\mu_O + q(E_{VBM} + E_F), \quad (3.5.3)$$

For the antisite, for Cu_O, $n_1 = -1, n_2 = 1$ and for O_{Cu}, $n_1 = 1, n_2 = -1$. So, Equation (3.5.1) becomes

$$\Delta H^f(Cu_O,0) = E(Cu_O,0) - E(P) - (\mu^0_{Cu} + \Delta\mu_{Cu}) + (\mu^0_O + \Delta\mu_O) + q(E_{VBM} + E_F), \quad (3.5.4)$$

$$\Delta H^f(O_{Cu},0) = E(O_{Cu},0) - E(P) + (\mu^0_{Cu} + \Delta\mu_{Cu}) - (\mu^0_O + \Delta\mu_O) + q(E_{VBM} + E_F). \quad (3.5.5)$$

For the interstitial defect, for I_{Cu}, $n_1 = -1, n_2 = 0$, and for I_O, $n_1 = 0, n_2 = -1$. Then, Equation (3.5.1) becomes

$$\Delta H^f(I_{Cu},0) = E(I_{Cu},0) - E(P) - (\mu^0_{Cu} + \Delta\mu_{Cu}) + q(E_{VBM} + E_F), \quad (3.5.6)$$

$$\Delta H^f(I_O,0) = E(I_O,0) - E(P) - (\mu^0_O + \Delta\mu_O) + q(E_{VBM} + E_F). \quad (3.5.7)$$

The total energies of perfect supercell and supercell with defect can be calculated by VASP. They can be viewed as constant at different growth conditions. However, the chemical potentials of elements depend on the growth conditions, in this case, which can be Cu rich or O rich in a vacuum-based environment, and anything in between. Initially, the chemical potentials of Cu and O are taken as that of Cu bulk and O_2, which are $\mu_{Cu} = -4.09\text{eV}$, $\mu_O = -7.98\text{eV}$

$$2\Delta\mu_{Cu} + \Delta\mu_O = \Delta H_f(Cu_2O) = -2.09\text{eV}, \quad (3.5.8)$$

where $\Delta H_f(Cu_2O)$ is the formation entholpy per molecule of Cu_2O,

Under Cu-rich conditions, Cu is assumed to be in a thermodynamic equilibrium with bulk Cu and, therefore, $\Delta\mu_{Cu} = 0$, then, $\mu_{Cu} = \mu_{Cu}^{0} = -4.09\text{eV}$. For the chemical potential of O, $\Delta\mu_{O} = -2.09\text{eV}$, then $\mu_{O} = \mu_{O}^{0} + \Delta\mu_{O} = -10.07\text{eV}$. Evidently, the lower limit of μ_{O} is limited by Cu metal formation. On the other side, the upper limit of μ_{O} is limited by CuO formation:

$$\Delta\mu_{Cu} + \Delta\mu_{O} = \Delta H_{f}(CuO) = -1.73\text{eV}, \qquad (3.5.9)$$

which leads to $\Delta\mu_{Cu} = -0.36\text{eV}$, $\Delta\mu_{O} = -1.37\text{eV}$. Therefore, when the environment of O move to the O-rich condition, $\mu_{Cu} = -4.45\text{eV}$, $\mu_{O} = -9.35\text{eV}$. Once the chemical potential of O is above this value, CuO will form. Now that the chemical potentials of Cu and O in both conditions are obtained, the formation energies of defects can be calculated by Equations (3.5.2-3.5.7).

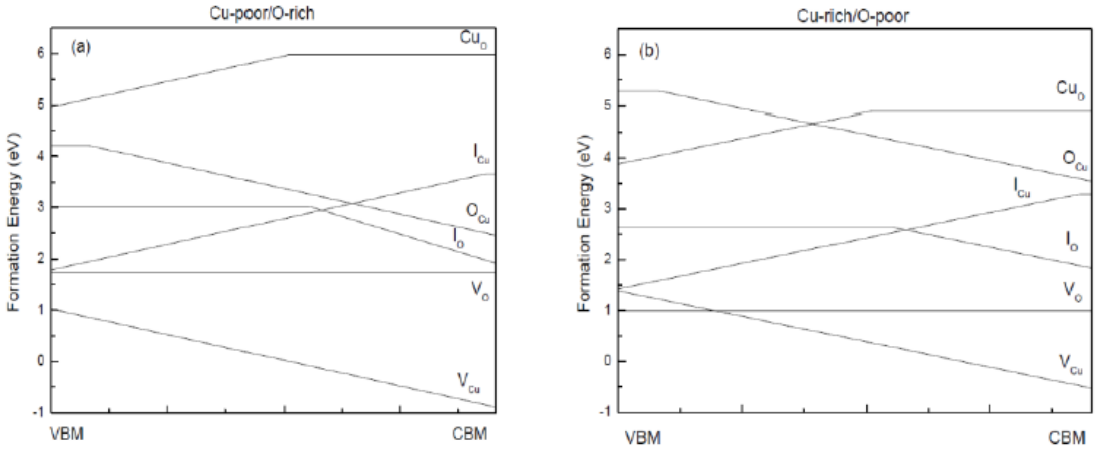

Figure 3.4 Formation energies as a function of Fermi level for native point defects in Cu_2O under (a) O-rich and (b) Cu-rich conditions in vacuum based growth. The zero point of the Fermi level corresponds to the top of the valence band. Only segments corresponding to the lowest-energy charge states are shown. The slope of these segments indicates the charge. Kinks in the curves indicate transitions between different charge states.

Based on the above data, the formation energies of various point defects in Cu_2O as a function of the Fermi level, which varies from conduction band minimum (VBM) to the conduction band minimum (CBM), are shown in Figure 3.4. Only the lowest-energy states for each charge state are shown. For interstitial sites, only the sites with the lowest formation energy are shown here.

Under the O-rich condition, V_{Cu} has the minimum formation energy which indicates its p-type character. The negative slope for V_{Cu} indicates that the Cu vacancy prefers to capture an electron. Therefore, copper vacancy acts as an acceptor in Cu_2O. The formation energies of the interstitials are significantly higher than that of copper vacancy, suggesting a less important role for the interstitials. The formation energy of antisite defect CuO is even higher. For oxygen vacancy, V_O, the present calculation shows that it prefers to be in its neutral charge state.

Under the Cu-rich condition, V_{Cu} has the lowest formation energy as well, and its value is slightly larger than that under the Cu-rich condition. On the other hand, the formation energies of other defects decrease as compared to the corresponding values under the O-rich condition. At the two extreme conditions, V_{Cu} has always the lowest formation energy, indicating that there is spontaneous formation of Cu vacancy during the growth of crystalline Cu_2O in the vacuum-based environment, leading to an intrinsic p-type material. These results agree well with experimental results [100-103] and previous theoretical studies [104-106].

Actually, the chemical potential of Cu range from -4.09 eV to -4.45 eV in vacuum condition. Among the three n-type defects, I_{Cu} has the lowest formation energy. However, the formation energy of V_{Cu} is lower than I_{Cu} on all this range. By using thermal oxidation or sputtering in vacuum conditions, it is impossible to obtain the intrinsic n-type Cu_2O. So the electrochemical deposition in solution conditions should be considered.

3.5.2 Formation Energies in Solution Conditions

In solution condition, Cu exists as a form of ion, which is difficult to exactly determine its chemical potential. But it can be obtained from the reaction equation in a solution. From Eq. (3.1.4), we can get the following equation at equilibrium,

$$2\mu_{Cu} + 2\mu_{OH} = \mu_{Cu_2O} + \mu_{H_2O}. \qquad (3.5.10)$$

In a solution condition, the chemical potential of Cu_2O and H_2O can be viewed as constant. If pH is changed, the concentration of OH^- is changed, and further the chemical potential of OH^- will change. Therefore, we try to determine the chemical potential of OH^- in

order to obtain the chemical potential of Cu. An assumption is made that OH is considered instead of OH^- in the following discussions [24]. Here, two limit conditions are considered, pH=0 and pH=14, which corresponds to strong acid and strong basic, respectively [18]. At pH=14, OH^- has its highest chemical potential since OH^- exists in the solution with the maximum activity as compared to the minimum activity in the extremely acidic environment. At pH=0, OH^- is combined easily with H^+ to form a relatively stable H_2O molecule, resulting in a lowest chemical potential for OH^-. To simplify the problem, we just consider OH instead of OH^- in our following discussions. At the extremely basic limit, OH^- is rich and the chemical potential of $OH^-$was approximated as the same as that of isolated OH. The total energy of OH was found to be -11.70 eV. This was regarded as the upper bound. At the extremely acid limit, H^+ is rich and its potential is taken as that of H^+, which is 0 for an isolated atom. Then the chemical potential of OH^-equals to that of water at pH=0, which is -18.85eV. Then the chemical potential of copper can be determined by Equation (3.5.12) and it ranges from -6.85 eV to 0 eV. It cannot beyond the isolated Cu atom value, which is zero in our scale.

During the calculation, we assume that the chemical potential of OH^- varies linearly according to the change of pH value. Therefore, the chemical potential of Cu also changes linearly. As shown in Figure 3.5 (a) refers to the range of Cu chemical potential in vacuum condition while (b) refers to the range in solution condition.

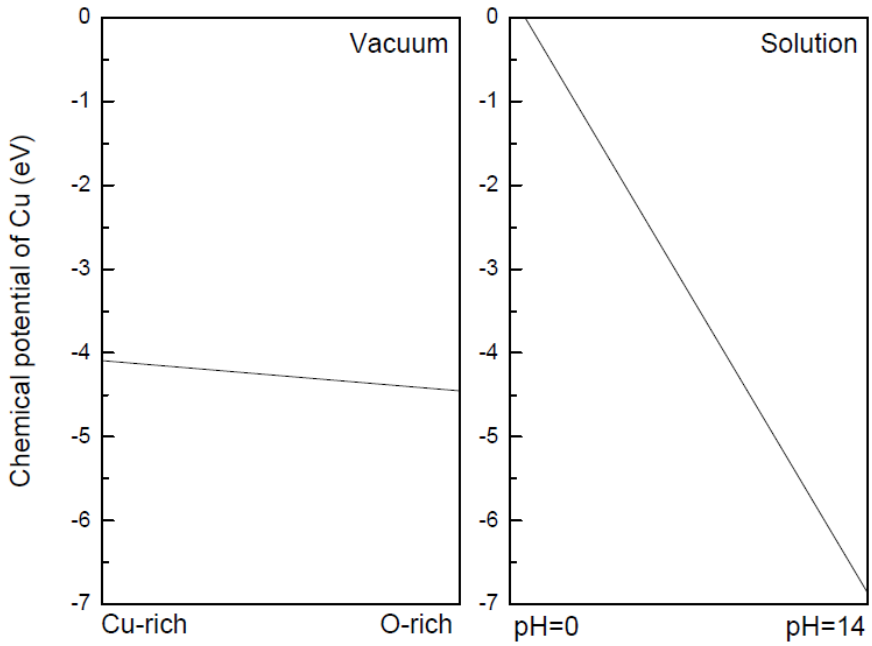

Figure 3.5 The range of chemical potential of Cu (a) at vacuum condition, (b) at solution condition. (a) The two limit values are obtained at Cu-rich and O-rich conditions. (b) The two limit values are obtained at pH=0 and pH=14, which correspond to the strong acid solution and strong basic solution.

Following the linear relation between the chemical potential of Cu and the pH value, we can easily calculate the specific value of μ_{Cu} at certain pH value. Here, the chemical potential of Cu at pH=4 is chosen for the n-type Cu_2O while that of Cu at pH=9 is taken for p-type Cu_2O. The chemical potential of Cu is -1.74eV at pH=4 and -4.30eV at pH=9, respectively.

As we obtained the chemical potential of Cu, then the chemical potential of O can be obtained from

$$2\mu_{Cu} + \mu_O = \mu_{Cu_2O} \qquad (3.5.13)$$

then by using the Equations (3.5.2-3.5.7), the formation energies of native point defects corresponding to three different solution environments can be calculated, which are presented in Figure 3.6, Figure 3.7, and Figure 3.8. They show a change in conduction mechanism of Cu_2O in solution environment at different pH value. Figure 3.6 shows defect formation energies in Cu_2O at pH value of 9, with the chemical potential of Cu at -4.30 eV. At pH=9, V_{Cu} is the dominant defect with the lowest formation energy among these intrinsic defects. From the view

of the formation energy, I_{Cu} is the lowest n-type defect. But it is still much higher than p-type V_{Cu}. They will be easily compensated by other p-type native defects.

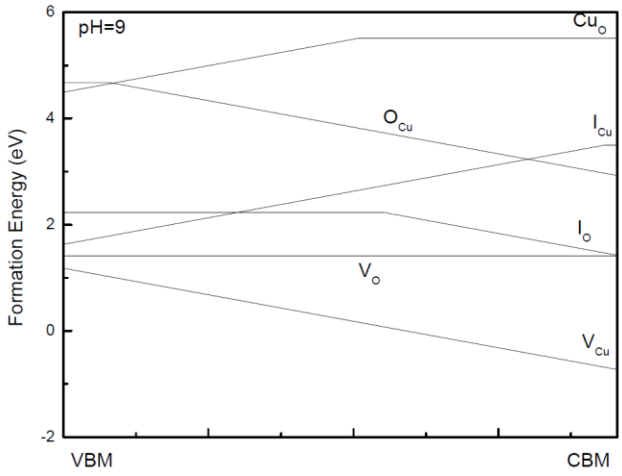

Figure 3.6 Formation energies as a function of Fermi level for native point defects in Cu_2O in the solution with pH=9.

When the pH value decreases to about 6 as shown in Figure 3.7, the chemical potential of Cu increased to -2.76 eV. At this pH value, V_O has the lowest formation engery. However, V_O, as a neutral defect, cannot contribute to the conductivity of Cu_2O. The formation energies of other p-type (V_{Cu}) and n-type (I_{Cu} and CuO) defects vary according to the position of the Fermi level. So at this pH value, the conductivity could be amphoteric, depending on the Fermi level.

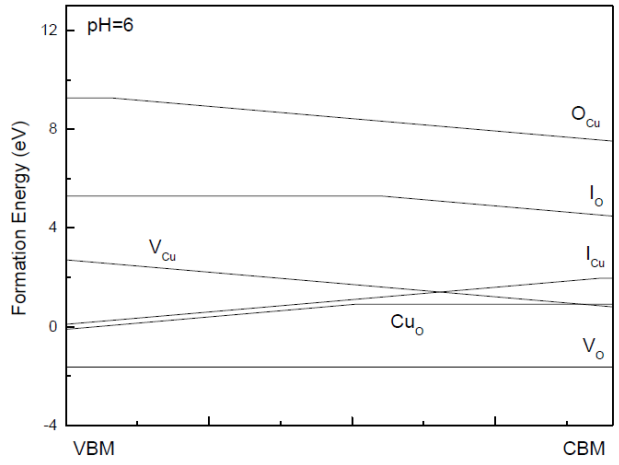

Figure 3.7 Formation energies as a function of Fermi level for native point defects in Cu2O in the solution with pH=6.

When the pH value further decreases to 4, V_O still has the lowest formation energy as it is shown in Figure 3.8.

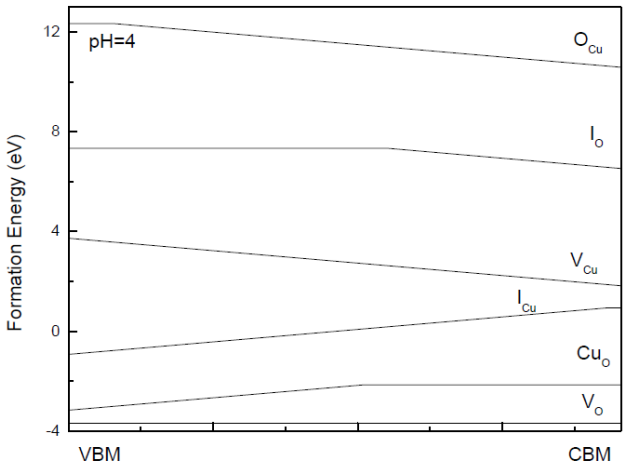

Figure 3.8 Formation energies as a function of Fermi level for native point defects in Cu_2O in the solution with pH=4.

The formation energy of Cu_O becomes much lower than that of the formation energy of I_{Cu}. Due to the low formation energy, the extra electrons provided by Cu_O will not be compensated by V_{Cu}. We claim that n-type Cu_2O can be obtained in solution with low pH value while p-type Cu_2O can be obtained in solution with high pH value. In Scanlon's [92] paper, they denied the existence of n-type Cu_2O. However, the antisite defect is not considered in their research, which provides n-type conductivity in acidic solution. This trend of change of conductivity with the pH value in the growth solution is in good agreement with experiment [23].

3.6 Summary

The structural and electronic properties of Cu_2O have been studied by first principles studies. Also, the formation energies of native point defects in undoped Cu_2O have been calculated by HSE hybrid functional theory in two conditions, which are vacuum-based condition and solution-based condition. All the intrinsic defects are considered here. Copper vacancy always has the lowest formation energy in both Cu-rich and O-rich conditions in vacuum based conditions. Copper vacancy provides p-type conductivity in Cu_2O. This result agrees well with

previous experimental [101] and theoretical results [104]. However, the resistivity is very high because that its conductivity is via a polaronic, hole-hopping mechanism [104–106] and the mobility of carriers is very slow. In Chapter 5, we will discuss the p-type doping in Cu_2O to improve the conductivity of Cu_2O.

In the solution-based condition, the type of conductivity varies with the change of pH value. When pH=9, V_{Cu} has the lowest formation energy and a highest concentration, which provide p-type conductivity. When pH is lowered to 6, the conductivity is amphoteric, depending on the position of the Fermi level. When pH further decreases to 4, the antisite defect Cu_O has the lowest formation energy, which is responsible for the n-type conduction. The theoretical results are in good agreement with experimental results [23-24]. From the above theoretical study, n-type Cu_2O can be obtained in solution with low pH value.

CHAPTER 4

N-TYPE DOPING IN COUPROUS OXIDE

4.1 Introduction

So far, both intrinsic n-type and p-type Cu_2O has been realized by experiments and also been verified from the theoretical study [23-24]. However, studies of the intrinsic Cu_2O p-n junctions revealed highly resistivity in both of n-type and p-type Cu_2O, leading to a low efficiency of about 0.1% for a solar cell [107]. To improve the conductivity of Cu_2O and hence the efficiency of the p-n junction, doping of shallow level impurities is a natural option. In 1982, Olsen et al. [21] fabricated p-type Cu_2O by thermal oxidation. This experiment was conducted in two conditions. One is in an Ar-O_2 only and another is in Ar-O_2 with chlorine vapor. The resistivity in the first condition is in the 1000-2000 $\Omega \cdot \mathrm{cm}$. The resistivity can be reduced after the Cl_2 vapor flow into the furnace. In 2010, Han et al. [108] reported that n-type doping of Cu_2O films by chlorine (Cl) are fabricated by electrochemical deposition. They claims that amount of Cl incorporated into the Cu_2O film affects the resistivity, lowering it up to 5 orders of magnitude. The lowest resistivity in the experiment is 7 $\Omega \cdot \mathrm{cm}$, suitable for solar cell applications. Researchers also try to substitute the Cu by selected 2 valence metal atoms, such as Zn, Mg, and so on. In 2003, Kale et al. [109] used Co and Zn and other elements co-doping in Cu_2O and found that co-doping with Zn causes decrease in resistivity. In 2007, Atay et al. [110] conducted Mg incorporation in Cu_2O and found that Mg incorporation has an affirmative effect on the optical and especially structural properties, but not a strong effect on the electrical properties.

However, the actual doping mechanism is not clear yet. In Cu_2O unit cell, the dopant not only could substitute an oxygen atom or a copper atom, but also could go to the interstitial sites. If the doped Cu_2O is p-type, the Cl atom probably occupies one of the interstitial sites, which provides a hole. If the doped Cu_2O is n-type, the Cl atom substitutes an O atom in Cu_2O,

which provide an electron. The reason for Zn incorporation to decrease conductivity we assume is that one Zn atom substitutes one Cu atom, which provide one extra electron and increase the conductivity. As for Mg, it also has two electrons in the outmost shell as Zn. The possibility of these doping are entirely depends on their formation energies. To study these doping quantitatively, a first principles study is conducted for the possible dopant in Cu_2O. The dopants considered here include halogen atoms and some selective two-valence metal atoms. I hope our theoretical research will provide guidance to further experimental researches on Cu_2O. The halogen atom (that refers to F, Cl, Br) is used to substitute the O atom, which will provide one extra electron. The metal atoms include Zn, Ca, and Mg, which has similar size as Cu atom. They are used to substitute the Cu atom, which also provide one extra electron. The interstitial sites of dopants are also considered, since they are also possible local minima.

4.2 Computational Details

The calculations in this chapter were also performed using the VASP package [37-41]. The GGA was also adopted initially. The PAW potential for Cu was generated from the atomic configuration of $[Ar]3d^{10}4s^1$. For O, the atomic configuration to generate the PAW potential was $[He]2s^2 2p^4$. For the dopants of F, Cl and Br, the atomic configuration to generate the PAW potential was $[He]2s^2 2p^5$, $[Ne]3s^2 3p^5$ and $[Ar]4s^2 4p^5$, respectively. For the dopants of Zn, Ca, and Mg, the atomic configuration to generate the PAW potential was $[Ar]3d^{10}4s^2$, $[Ne]3s^2 3p^6 4s^2$, and $[Ne]4s^2$, respectively. The geometry optimization after an impurity introduced in Cu_2O is conducted using GGA-PBE calculations. The total energy and the final electronic structure calculations are conducted using GGA-PBE and the HSE hybrid density functionals [42-43] approach. In the hybrid functional, the same parameters are set as Chapter 3.

4.3 Formulas of Formation Energy and Determination of pH Value

Here, the defects considered include both substitutional defects and interstitial defects. The formation energies of holagen defects and metal defects are introduced individually. First, the formation energy of a substitutional halogen defect can be expressed as

$$\Delta H^f(X_O) = E(X_O) - E(P) + \mu_O - \mu_X + q[E_{VBM} + \varepsilon_F + \Delta v(D)], \quad (4.3.1)$$

where X refers to the halogen atom, which is F, Cl and Br. X_O represents one halogen atom replace one O atom in Cu_2O. $E(X_O)$ is the total energy of the defect supercell doped by halogen atom and $E(P)$ is the total energy of perfect cell. μ_O and μ_X are the chemical potential of O atom and halogen atom, respectively.

The formation energy of an interstitial halogen atom defect can be expressed as

$$\Delta H^f(X_I) = E(X_I) - E(P) - \mu_X + q[E_{VBM} + \varepsilon_F + \Delta v(D)], \quad (4.3.2)$$

where X_I represents that one halogen atom goes into an interstitial site in Cu_2O.

Next, the formation energy of a substitutional metal atom can be expressed as

$$\Delta H^f(Y_{Cu}) = E(Y_{Cu}) - E(P) + \mu_{Cu} - \mu_Y + q[E_{VBM} + \varepsilon_F + \Delta v(D)], \quad (4.3.3)$$

where Y refers to the metal atom, which is Zn, Ca and Mg. Y_{Cu} represents that one metal atom replace one Cu atom in Cu_2O. $E(Y_{Cu})$ is the total energy of the defect supercell doped by halogen atom and $E(P)$ is the total energy of perfect cell. μ_{Cu} and μ_Y are the chemical potential of Cu atom and metal atom, respectively.

The formation energy of an interstitial metal defect can be expressed as

$$\Delta H^f(Y_I) = E(Y_I) - E(P) - \mu_{Cu} + q[E_{VBM} + \varepsilon_F + \Delta v(D)], \quad (4.3.4)$$

where Y_I represents that one metal atom goes into an interstitial site in Cu_2O.

In this chapter, our focus is on the n-type doping in Cu_2O. From the previous chapter, n-type Cu_2O can be produced in the solution with low pH value as discussed in Chapter 3. Therefore, an optimal pH is needed to determine, which provides the best condition for n-type doped Cu_2O. In the calculation of formation energy, the chemical potential of Cu plays an important role. After calculation, pH=4 is taken for halogen atom and Ca, Mg, while pH=6 is taken for Zn. At pH=4, ZnO will be dissolved.

4.4 N-type Doping in Cu_2O by Halogen Atoms

4.4.1 Structural and Electronic Properties

In doped Cu_2O, 2×2×2 unit cells are adopted to avoid interaction of dopants due to the periodical boundary condition. For substitutional dopant, one halogen atom will substitute one O atom in the supercell. Here, the O atom at the origin (0, 0, 0) is chosen. The distances of the nearest neighbor (n.n.) of the dopant and dopant before and after doped are listed in Table 4.1. It is obvious that the larger the atomic size of the dopant is, the further the n.n. Cu atoms are pushed away, creating higher local stress. F is in the same line in the periodic table as O atom so that the doping leads to very small change between F and its neighbors. But for Cl and Br, the doping leads to a larger change due to the bigger size of atoms. The structure of tetrahedron of 4 Cu atoms surrounding the dopant does not change after doped, which means that the changes in 4 neighboring Cu atoms are in the same amount. For the second and third nearest neighbors, there is little change on the distance between neighboring atoms.

Table 4.1 The distance of the first nearest neighbors and the change from an ideal Cu–O bond length in Cu_2O after the O substitution by halogen atoms

Dopant	First nearest neighbor (Å)	Change (%)
F	2.00	7.0
Cl	2.14	14.4
Br	2.70	44.4

As a comparison, interstitial defect is also considered. For interstitial defect, three non-equivalent interstitial sites with high symmetry have been considered in the calculation. They include two sites with a Td local symmetry, one at the face-center of the cubic unit-cell (T1) and one in the middle of the side of the cubic (T2), and one site with an octahedral local symmetry (O), which are shown in Figure 4.1. After geometry optimization, T2 has the lowest energy. The change of distance between atoms due to the interstitial defect is much larger than that caused by the substitutional defect. This trend agrees well with the trend of change of formation energy. The formation energy of interstitial defect is also much higher than that of substitutional defect.

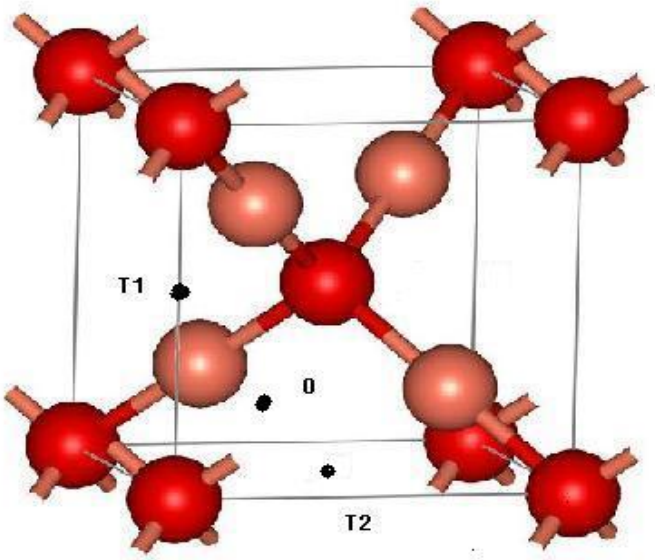

Figure 4.1 Sites for high symmetric interstitial defect (T1, T2 are the tetrahedral sites and O is the octahedral site)

4.4.2 Calculation of Formation Energies

Next, we will talk about the formation energy of defects. As stated earlier, all calculations of formation energy are conducted at pH=4, which is the best pH value for n-type Cu2O doped by halogen atom to form. This also agrees well with the experiment of preparation of n-type Cu_2O [108]. The formation energies of the three halogen dopants, i.e. F, Cl, and Br, both at the substitution site and at the interstitial site, as well as their charged states, are calculated. The upper and lower limits of the chemical potential of OH are calculated same as stated in Chapter 3 and range from –11.70 to –18.55 eV. Under the assumption that the chemical potential of OH linearly changes with the pH value, the chemical potential of OH is obtained for a given pH. To model an n-type solution growth environment, pH=4 is chosen, which gives the chemical potential of OH as -16.81 eV. This leads the chemical potential of Cu equal to -1.74 eV, from Equation (3.5.12) $2\mu_{\mathrm{Cu}} + 2\mu_{\mathrm{OH}} = \mu_{\mathrm{Cu_2O}} + \mu_{\mathrm{H_2O}}$, and the chemical potential of O -14.76 eV from Equation (3.5.17) $2\mu_{\mathrm{Cu}} + \mu_{\mathrm{O}} = \mu_{\mathrm{Cu_2O}}$. The formation energies of

copper halide can be calculated by VASP directly. Then the chemical potentials of F, Cl and Br are -9.60 eV, -8.02 eV, and -7.24 eV, respectively, which are calculated from the following equation,

$$\mu_{Cu} + \mu_X = \mu_{CuX}, \qquad (4.4.1)$$

where X refer to F, Cl and Br.

The formation energies of the three halogen dopants are plotted versus the Fermi level in the band gap, as shown in Figure 4.2. For each dopant at a specific site, only the lowest charge-state is drawn. For all the three dopants, the interstitials always have substantial higher formation energies than their substitutional counterparts. Therefore, the halogens are more stable on the substitution site in Cu_2O. Among the three, F has the lowest formation energy. The formation energy of Cl is higher, 0.74 eV at the conduction-band minimum (CBM), and Br has the highest, though still at a reasonable value of 1.31 eV at the CBM. This is consistent with the local structural relaxation they caused, as demonstrated in Table 4.1. Finally, the formation energy of Cu vacancy, V_{Cu}, is shown in Figure 4.2 (b) for comparison. V_{Cu} is a dominant p-type native defect in vacuum-based growth [92-93] and in the basic solution-based growth [24]. The value in Figure 4.2 (b) is at least 1 eV more than that of F and Cl dopants and about 0.8 eV higher than that of the Br dopant. This should prevent the halogen dopants from being compensated by the holes provided by V_{Cu}, since its concentration would be much lower, due to a much higher cost to form.

In a vacuum-based growth, V_{Cu} has very low formation energies both at Cu-rich/O-poor condition and Cu-poor/O-rich condition. At these low formation energies, V_{Cu} is abundant. Its shallow acceptor level will compensate any donors. To have an efficient n-type doping, the formation energy of V_{Cu} should be substantially higher. This must be true for the undoped n-type Cu_2O, though its conduction mechanism is still debatable [92]. The assumption used in the theoretical work for the vacuum-based growth, in which the chemical potential of copper in materials is capped by that of metallic Cu, may not be true in an electrochemical growth. After

all, the metal is ionized in the electrolyte.

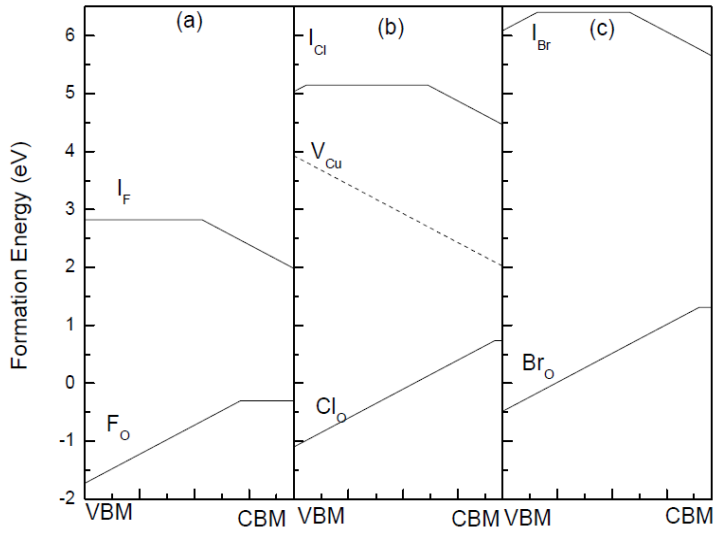

Figure 4.2 Formation energies of defects of Cu_2O as a function of the Fermi level at pH=4. Formation energies of F, Cl and Br at neutral and charge=+1 states are given in panel a, b and c, respectively. And the formation energy of Cu vacancy is given as dashed line in panel b.

The single-particle defect levels of the substitutional F, Cl, and Br are shown in Figure 4.3. Though all of them provide a donor level in the band gap, which is calculated as 1.91 eV, the impurity level due to Cl substitution of O is shallower than the other two, only 0.17 eV below the CBM. This is also consistent with the charge state (+1/0) transition shown in Figure 4.2. The electron on this level can be easily excited by thermal energy to the bottom of the conduction band. In Figure 4.4, we have presented the projected density-of-state of the Cu_2O crystal. It clearly shows that the bottom of the conduction band is dominated by the oxygen 3 s-states. The electrons excited from the shallow impurity levels can then enhance the n-type conductivity, as observed in the very recent experiment [111], where the resistivity was reduced by over 5 orders of magnitude in the Cl-doped Cu_2O.

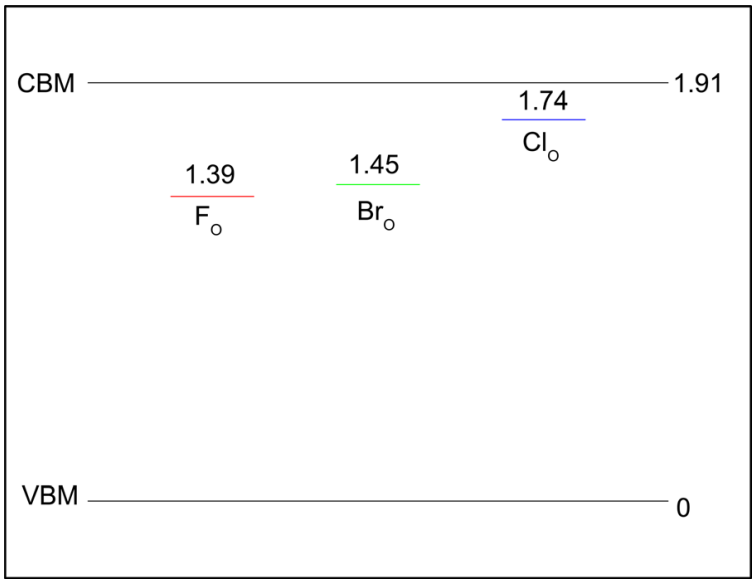

Figure 4.3 The single-particle impurity levels. The single particle impurity levels of the substitutional F, Br, and Cl are shown, measured from VBM in eV. The Cl dopant has the shallowest level, about 0.17 eV below the CBM.

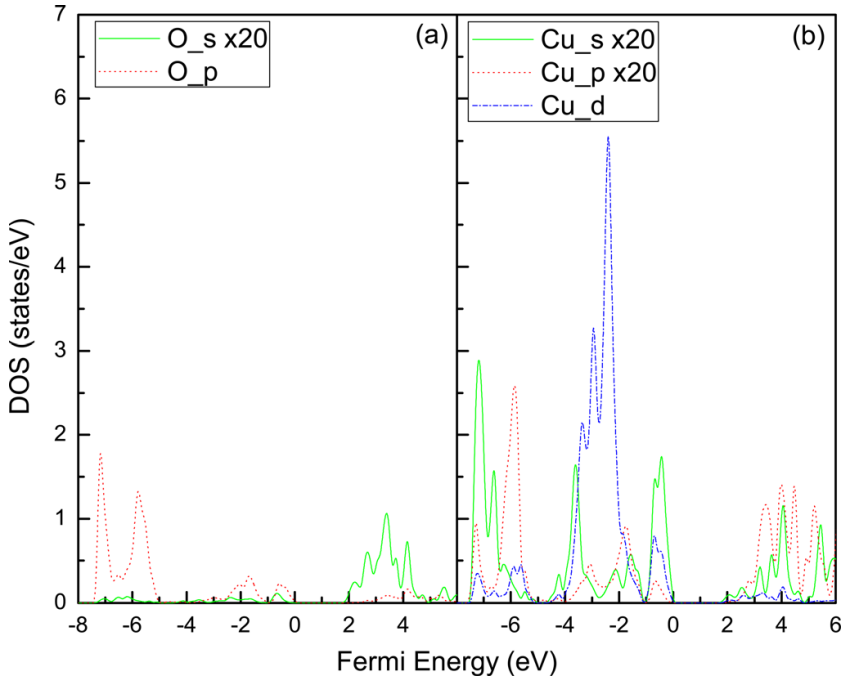

Figure 4.4 The projected density-of-state (DOS). The DOS of crystal Cu_2O projected by angular-momentum near the band gap are plotted VS the Fermi level, which has the zero point at the VBM. Panel (a) is for the oxygen site projection, where the s-component is amplified by 20 times. Panel (b) is for the copper site projection, where both the s- and p-components are amplified by 20 times.

4.5 N-type Doping in Cu_2O by Selected Metal Atoms

In the above part, we have successfully explained the n-type Cu_2O doped by halogen atom in solution condition by first principles calculation. In this part, we will study the substitution of Cu atom by selected metal atoms to obtain n-type Cu_2O semiconductor.

4.5.1 Structural and Electronic Properties

When a dopant is introduced in the supercell, the likely sites are all considered. It includes the substitution of a Cu atom and several high symmetrical interstitial sites. The substitutional impurity was considered first. It was introduced by replacing a Cu atom with a 2-valence metal atom (Zn, Ca, or Mg) in the supercell. Then, all the atoms were allowed to relax according to the Hellmann-Feynman forces until the change of the total energy was less than 0.001 eV/cell. After the substitution, the surrounding atoms have the substantial relaxation. The distances of the first nearest neighbor (n.n.) of the dopants and the change from an ideal Cu–O distance (1.87 Å) in Cu_2O is listed in Table 4.2. The ionic radius of Zn, Ca, and Mg are 0.40Å, 1.00Å, and 0.49Å, respectively [18]. It is obvious that the larger the atomic size of the dopant is, the further the n.n. Cu atoms are pushed away, creating higher local stress. This is also consistent with the cost of their formation.

Table 4.2 The distance of the first nearest neighbors and the change from an ideal Cu–O bond length in Cu_2O after the O substitution by metal atoms

Dopant	First nearest neighbor (Å)	Change (%)
Zn	1.91	2.14
Ca	2.18	16.58
Mg	1.92	2.67

Here, the interstitial defects are also considered for a comparison with substitutional defects. Similarly as the above halogen dopant, the tetrahedral site on the middle of the side are used to calculation the formation energy of the interstitial defects, which have the lowest formation energy among these interstitial sites.

4.5.2 Formation Energies in Vacuum Conditions

We considered the formation energy of extrinsic metal defect from two conditions, which are vacuum condition and solution condition.

In vacuum condition, we follow the method for undoped Cu_2O in Chapter 3. Here, we take two limit conditions, which are Cu-rich/O-poor and Cu-poor/O-rich. The same value of chemical potential of Cu and O atom are used as Chapter 3. Now we begin to calculate the chemical potential of metal atoms. The total energy of the metal oxides can be obtained by calculation in VASP. The metal oxides refer to ZnO, MgO and CaO. According to the following equation, the chemical potential of metal atoms can be calculated by

$$\mu_X + \mu_O = \mu_{XO}, \qquad (4.5.1)$$

where X refer to Zn, Mg, or Ca.

Based on the above data, the formation energies of various point defects in Cu_2O as a function of the Fermi level (ε_F), which varies from conduction band minimum (VBM) to the conduction band minimum (CBM), are shown in Figure 4.5. For substitutional defect, which easily loose one electron, the charge states considered here are q=0 or +1. For interstitial defects, the charge states we considered here are q=-1, 0 or +1. Only the lowest energy state at a given ε_F is shown. Also, the formation energy of V_{Cu} is shown for comparison. Copper vacancy acts as an acceptor in Cu_2O. Figure 4.5(a) shows the formation energies of all the extrinsic n-type defects and copper vacancy for different charge states calculated with HSE under Cu-poor/O-rich condition. The formation energies of Zn_{Cu}, Ca_{Cu}, and Mg_{Cu} are 2.70eV, 3.29eV, and 3.62eV at CBM. They are all higher in energy than that of V_{Cu}. This trend of increase of the formation energies is consistent with the change of Cu-O bond after doping, which means that the larger the size of dopant is, the higher the corresponding formation energy is. For interstitial sites, their formation energies are much higher than that of substitutional sites, which is difficult to form. Figure 4.5 (b) shows the formation energies of defects under Cu-rich/O-poor condition. The formation energies of Zn_{Cu}, Ca_{Cu}, and Mg_{Cu}

decease to 2.34eV, 2.93eV, and 3.26eV, respectively. Although the formation energies of defects are affected by different conditions, the formation energy of V_{Cu} is still much lower than that of dopants when ε_F close to CBM as n-type conductivity condition. V_{Cu} is still the dominant defect in Cu_2O and has a high concentration.

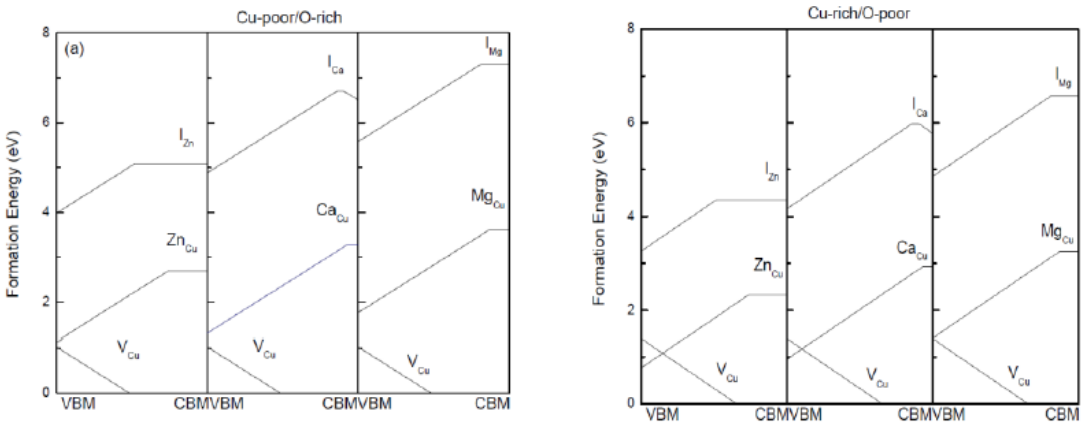

Figure 4.5 Formation energies of metal defects in Cu_2O under (a) Cu-poor/O-rich and (b) Cu-rich/O-poor conditions in vacuum based growth. The zero point of the Fermi level corresponds to the top of the valence band. Only segments corresponding to the lowest-energy charge states are shown. Kinks in the curves indicate transitions between different charge states.

As these results clearly show that at both of Cu-poor and Cu-rich conditions, the defect chemistry of Cu_2O will still be dominated by V_{Cu}, the extrinsic metal defects are difficult to form in the vacuum conditions. In other words, the metal defects will be compensated by V_{Cu} once they form. Referring to the method for n-type Cu_2O without doping, doping in Cu_2O of these selective metal atoms in Cu_2O by controlling the pH value of the solution will be studied next.

4.5.3 Formation Energies in Solution Conditions

In our calculation, we still use the same consideration in Chapter 3. In Chapter 3, it have been calculated that the chemical potential of copper ranges from -6.85 eV to 0 eV when the pH varies. Different pH values are used to calculate the formation energies of metal dopants and V_{Cu}. To make Cu_2O an n-type semiconductor, one requirement has to be met that the formation energies of n-type extrinsic defect must be lower than that of V_{Cu}. After our calculation, pH=6 is taken for Zn and pH=4 is taken for Mg and Ca. As we discussed above, the

chemical potential of Zn is so large that Zn^{2+} is not stable in Cu_2O at pH=4 and cannot coexist with Cu_2O as a form of ZnO. Ca and Mg are doped at pH=4 because they are stable at such condition with low formation energies. At such conditions, the chemical potentials of Zn, Mg, Ca are -0.95eV, -2.11eV, and -1.20eV, respectively.

The formation energies of the three metal dopants are plotted versus the Fermi level in the band gap, as shown in Figure 4.6. For each dopant at a specific site, only the lowest charge-state is drawn. For all the three dopants, the interstitials always have substantial higher formation energies than their substitutional counterparts, which have good agreement with that calculated in vacuum conditions. Therefore, the dopants are more stable on the substitution site in Cu_2O.

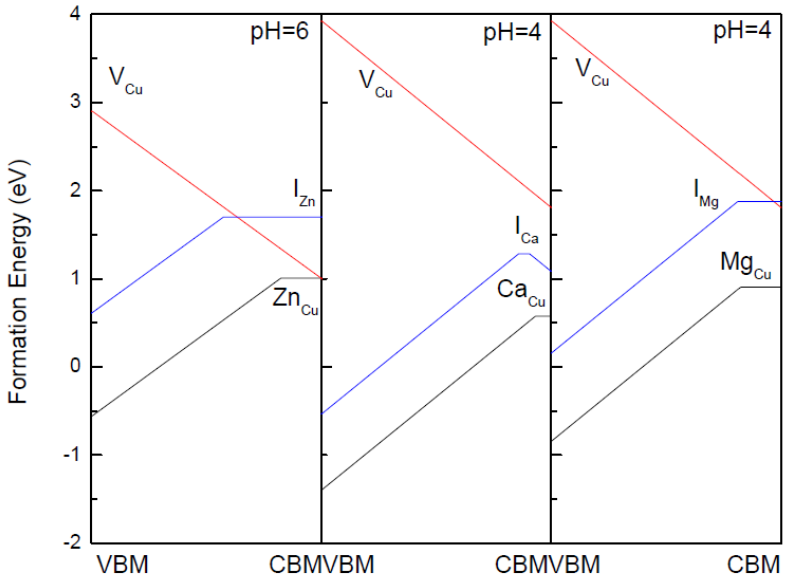

Figure 4.6 Formation energies of defects of Cu_2O as a function of the Fermi level at pH=6 for Zn and at pH=4 for Ca and Mg. Formation energies of Zn, Ca and Mg at neutral and charge=+1 states are given in panel a, b and c, respectively. And the formation energy of Cu vacancy is given.

Finally, the formation energy of Cu vacancy, V_{Cu}, is shown in Figure 4.6 for comparison. V_{Cu} is a dominant p-type native defect in vacuum-based growth [92] as stated above. In solution-based condition, V_{Cu} has higher formation energy than that of the dopant defects at

these two selected pH value, which facilitates the formation of metal dopant defects. This prevents the metal dopants being compensated by the holes provided by V_{Cu} since the concentration of V_{Cu} should be much lower. Compared with Mg, the formation energy of Ca is lower, which is about 0.61 eV at the bottom of conduction band. This means that Ca_{Cu} has a high concentration. Also, the transition level is shallower so that the extra electron can easily be excited to conduction band.

The single-particle defect levels of the substitutional, Zn, Mg and Ca are shown in Figure 4.7. Though all of them provide a donor level in the band gap, the impurity level of CaCu is shallower than the other two, only 0.11 eV below the CBM. This is also consistent with the charge state (+1/0) transition level shown in Figure 4.6. The electron on this level can be easily excited by thermal energy to the bottom of the conduction band.

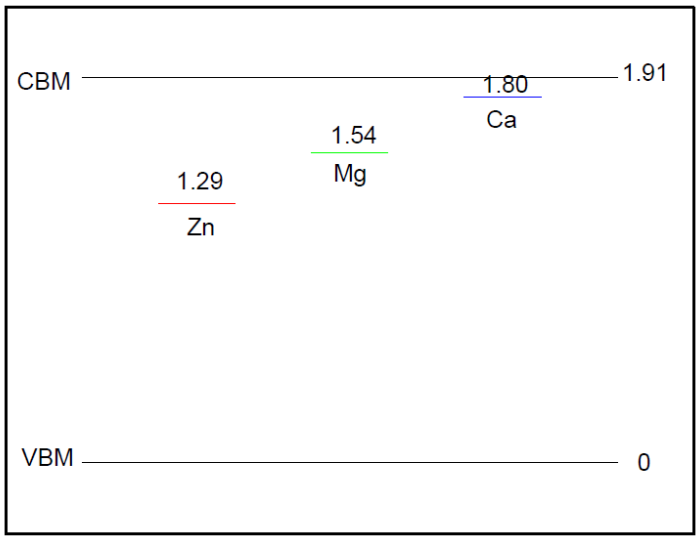

Figure 4.7 The single-particle impurity levels. The single particle impurity levels of the substitutional Zn, Ca, and Mg are shown, measured from VBM in eV. The Ca dopant has the shallowest level, about 0.11 eV below the CBM.

4.6 N-type Co-doping in Cu_2O by Cl and Ca

From the above analysis and discussion, we know that Cl is the best halogen dopant in three halogen atoms and Ca is the best metal dopant in three selected metal atoms. In this part, we try to study the co-doping of Cl and Ca in the Cu_2O supercell, which is still made

by 2X2X2 unit cells. In this supercell, one O atom is substituted by one Cl atom while one Cu atom is substituted by one Ca atom. According to the distance between these two dopants in the supercell, there are several different combinations. Several different separations have been considered. The total energies of Cu_2O with two defects are calculated by VASP. There is no significant difference between the formation energies of them, which is only 0.13 eV. The closest co-dopant with lower energy is taken to calculate the formation energy. Formation energy of co-doping is calculated by the following equation.

$$\Delta H^f = E(D) - E(P) + \mu_O - \mu_{Cl} + \mu_{Cu} - \mu_{Ca} + q[E_{VBM} + \varepsilon_F + \Delta v(D)] \qquad (4.6.1)$$

The chemical potentials of elements at pH=4 are used because that pH=4 is the best pH value for the formation of n-type Cu_2O from our study. The formation energies of Cl_O, Ca_{Cu}, and co-doping are shown in Figure 4.8.

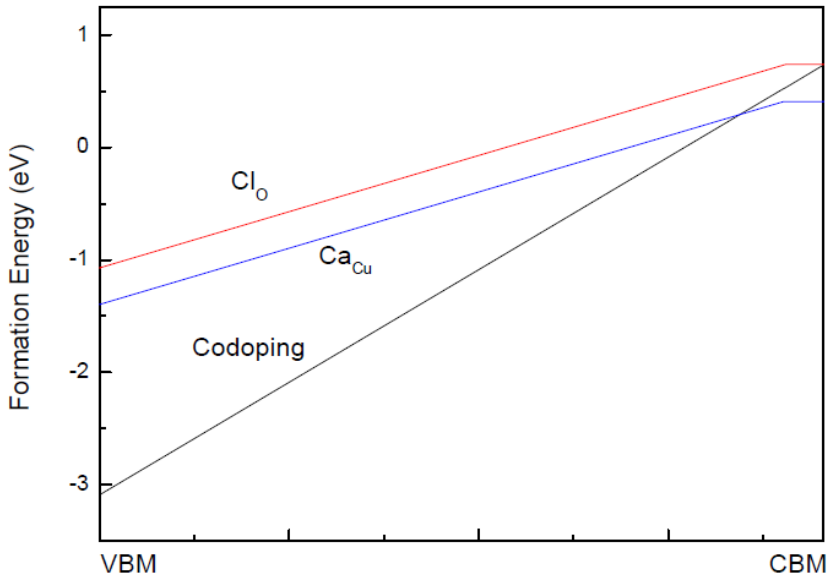

Figure 4.8 Formation energies of Cl_O and Ca_{Cu} and Cl_O-Ca_{Cu} as a function of the Fermi level at pH=4. Formation energies of Cl_O and Ca_{Cu} at neutral and charge=+1 states are given. And Formation energy of Cl_O-Ca_{Cu} at neutral and charge=+2 states are given.

One Cl_O provides one extra electron and the same does Ca_{Cu}. On the other side, one co-doping defect can provide two extra electrons. From the point of view of the number of

electrons provided by the defect, one co-doping defect is equivalent to combination of one Cl_O and one Ca_{Cu}. From Figure 4.8, the sum of the formation energies of one Cl_O and one Ca_{Cu} is larger than that of one co-doping defect at CBM, which means that co-doping is preferred to form when providing same number of electrons.

4.7 Summary

Cl_O and Ca_{Cu} The n-type doping by halogens in the Cu2O synthesized from an acidic solution environment has been studied by the first-principles calculations. The calculations show that the dopants of F, Cl, and Br are more stable in the substitutional sites of the O atoms with the low formation energies compared to the interstitial sites. The dopants present an n-type conduction behavior. The Cl has the shallowest donor level, only 0.17 eV below the bottom of the conduction bands. From the consideration of both the formation energy and the donor level, the Cl is the best dopant among the three. The results are in good agreement with the very recent experimental results. The bottom of conduction band has substantial O-3s band and Cu-4s band, which are non-localized.

Cl_O and Ca_{Cu} When the extra electron is excited to the conduction band, it will move rapidly and further improve the conductivity. The n-type doping by selected metal atoms in Cu2O at different pH value in a solution based environment has been studied by the first-principles calculations. Similarly, the calculated formation energies show that the dopants of Zn, Ca, and Mg are more stable in the substitutional sites of Cu atoms at corresponding solution condition. The formation energies are low. The dopants present an n-type conduction behavior. The donor levels are shallow. Ca has the shallowest donor level, only 0.11 eV below the bottom of the conduction bands. From the consideration of both the formation energy and the donor level, Ca is the best dopant among the three atoms. Similar to the Cl-doping case, the extra electron from Ca provided conductivity after excited to the conduction band.

Co-doping of Cl and Ca in Cu_2O is considered. The formation energy between co-doping and single doping are compared. It can be concluded from our calculation that co-doping

is preferred to form with providing same amount of electrons. We hope that our findings will stimulate experimental work aimed at n-type Cu_2O to verify our theoretical calculations.

CHAPTER 5

P-TYPE DOPING IN COUPROUS OXIDE

5.1 Introduction

Cu_2O naturally exists as a p-type semiconductor, where V_{Cu} provide the conductivity, as discussed in Chapter 3. To make it a Cu_2O homojunction and to improve its efficiency, n-type Cu_2O has been produced by the experiments and also been verified from the theoretical study [23-24]. However, the practical applications of Cu_2O materials have not been achieved to date due to the low efficiency and high resistivity. Though Cu_2O is intrinsically p-type semiconductor, in which V_{Cu} is dominant, however, its conductivity is via a polaronic, hole-hopping mechanism [104-106] and the mobility of holes is very poor. This type of conductivity is consistent with localized single particle levels deep in the band gap of the material. Shallow level p-type doping could introduce free carriers (holes) into Cu_2O instead of the polaron conductivity.

In this chapter, we focus on p-type doping to substitute an O atom by group V elements (N, P, As). Because group V elements have one less valence electron than O atom, it will provide a hole in the semiconductor. There are some experiments conducted on N-doped Cu_2O. Nitrogen gas is widely accepted as a nontoxic, low cost, and widely available gas. Also, N has a similar size as O atom. Therefore, N has been viewed as a promising candidate dopant in Cu_2O. In 2001, Ishizuka et al. [112] deposited the N-doped Cu_2O by reactive radio-frequency magnetron sputtering. In their experiments, they claimed that nitrogen has the effect of increasing holes density and to generate an acceptor level of 0.14 eV. Afterwards, Nakano [113] and Zhang [114] deposited N doped Cu_2O by sputtering. They demonstrated optical band gap widening of p-type Cu_2O thin films after N doping. However, the exact mechanism that leads to this phenomenon is still unknown. In the present chapter, the feasibility of p-type doping by group V elements will be studied at different solution based environments.

5.2 Computational Details

For p-type doping in Cu_2O, the calculations were also performed using the VASP package [37-41]. The PAW potential for Cu was generated from the atomic configuration of $[Ar]3d^{10}4s^1$. For O, the atomic configuration to generate the PAW potential was $[He]2s^2 2p^4$. For the dopants of N, P and As, the atomic configuration to generate the PAW potential was $[He]2s^2 2p^3$, $[Ne]3s^2 3p^3$ and $[Ar]4s^2 4p^3$, respectively. The geometry optimization after an impurity introduced in Cu_2O is conducted using GGA-PBE calculations. The total energy and the final electronic structure calculations are conducted using GGA-PBE and HSE hybrid density functionals approach. In the hybrid functional, the exchange part is a mixing of that of PBE and Hartree-Fock (HF), while the correlation part is still that of PBE. In the hybrid functional, the same parameters are set as Chapter 3.

5.3 Structural Properties

After the group V element is introduced in Cu_2O, the surrounding atom of dopant has changed to some extent. The substitutional impurity was considered first. For the sutstitutional defect, the distance of Cu-O bond is changed to some extent. Initially, the distance of Cu-O is 1.87 A. The distance for different dopants after substitution is shown in Table 6.1. After susbstitution of N, the distance between N and Cu is compressed by 2.1%. For the substitution of P and As, the distance is expanded by 13.4% and 18.2%, respectively. It is obvious that the larger the atomic size of the dopant is, the further the surrounding Cu atoms are pushed away, creating higher local stress. On the other hand, the group V element can also stay at a high symmetric interstitial site, which is either tetrahedral site or octahedral site, as we mentioned in the above chapter. The relaxation lead by the interstitial defect is more substantial.

Table 5.1 The distance of the first nearest neighbors and the change from an ideal Cu–O bond length in Cu_2O after the substitution

Dopant	First nearest neighbor (Å)	Change (%)
N	1.83	-2.1
P	2.12	13.4
As	2.21	18.2

5.4 Determination of the Chemical Potential

5.4.1 How to Determine the Chemical Potential of Cu

In this chapter, p-type doped Cu_2O in solution based environment is considered here. We already know that Cu_2O naturally exists as a p-type semiconductor, where Cu vacancy provides the conductivity in Chapter 3. P-type Cu_2O can always be obtained in vacuum condition. Also, intrinsic p-type Cu_2O can be fabricated at a basic pH value by electrochemical deposition. Here, p-type Cu_2O doped by group V elements is studied in a solution with a basic pH value. In this chapter, a moderate basic solutions with pH=9 and pH=10 are taken to calculate the chemical potential of OH-. Then the relevant chemical potentials of Cu can be obtained by Equation (3.5.12), which are -4.30eV and -4.81eV, respectively. They will be used in the following calculation. The details will be explained in the formation energy part.

5.4.2 How to Determine the Chemical Potential of Group V Atoms

Unlike the halogen atom and the metal atom, Group V elements can form compound either with Cu atom or O atom. The stability of two kinds of compounds is needed to determine which one is more stable in the solution condition. The possible compounds and their crystal structure are listed in Table 5.2. Cu_3N, Cu_3As, and As_2O_3 have a cubic crystal structure. N_2O_5 and Cu_3P possess hexagonal structure. And P_2O_5 has orthorhombic structure. The chemical potentials of the corresponding element in each compound are also listed. In the calculations, the integrations over the first Brillouin zone were made by using a 4X4X4 k-point set generated

according to the gamma-centered Monkhorst-Pack scheme [19] for unit cell. The lattice constant of compounds are optimized by DFT-GGA.

Table 5.2 The possible compounds and their corresponding chemical potential.

Elements	Copper compounds	Chemical potential (eV)	Oxides	Chemical potential (eV)
N	Cu_3N(cubic)	-8.52	N_2O_5(hexagonal)	-11.22
P	Cu_3P(hexagonal)	-5.67	P_2O_5(orthorhombic)	-14.30
As	Cu_3As(cubic)	-4.27	As_2O_3(cubic)	-9.03

After the geometry optimization, HSE functional is conducted to calculate the cohesive energy of these compounds. Then, the chemical potential of group V elements can be calculated by

$$\mu_X = (\mu_{compound} - n * \mu_Y)/m \qquad (5.4.1)$$

where X refers to the group V elements, Y refers to Cu or O atom, n and m is stoichiometric number. For example, for N_2O_5,

$$\mu_N = (\mu_{N_2O_5} - 5\mu_O)/2 \qquad (5.4.2)$$

After the chemical potentials of Cu and O are substituted into the above equation, the chemical potentials of group V elements are obtained. From our calculation, at pH=9, the chemical potential of N atom is -11.22eV in N_2O_5 while that is -8.52eV in Cu_3N. For P, the chemical potential of N atom is -14.30eV in P_2O_5 while that is -5.67eV in Cu_3P. For As, the chemical potential of N atom is -9.03eV in As_2O_3 while that is -4.27eV in Cu_3As. Obviously, the group V elements have smaller chemical potential in oxide than that in copper compound. Therefore, it can be concluded that group V elements prefer to form compound with O in solution based environment. Experiment [113] also shows that the N is difficult to combine with

Cu, which supports our conclusion. Thus, the chemical potential of group V elements is calculated by their corresponding oxide.

5.5 Calculation of Formation Energies

Here, the dopants considered include both substitutional and interstitial sites. First, the formation energy of a substitutional site can be expressed as

$$\Delta H^f(X_O) = E(X_O) - E(P) + \mu_O - \mu_X + q[E_{VBM} + \varepsilon_F + \Delta v(D)], \qquad (5.5.1)$$

where X refers to the group V atom, which are N, P and As. X_O represents that one group V atom replace one O atom in Cu_2O. $E(X_O)$ is the total energy of the defect supercell doped by group V atom and $E(P)$ is the total energy of perfect cell. μ_O and μ_X are the chemical potential of O atom and group V atom, respectively. The formation energy of an interstitial defect can be expressed as

$$\Delta H^f(X_I) = E(X_I) - E(P) - \mu_X + q[E_{VBM} + \varepsilon_F + \Delta v(D)], \qquad (5.5.2)$$

where X_I represents that one group V atom goes into an interstitial site in Cu2O.

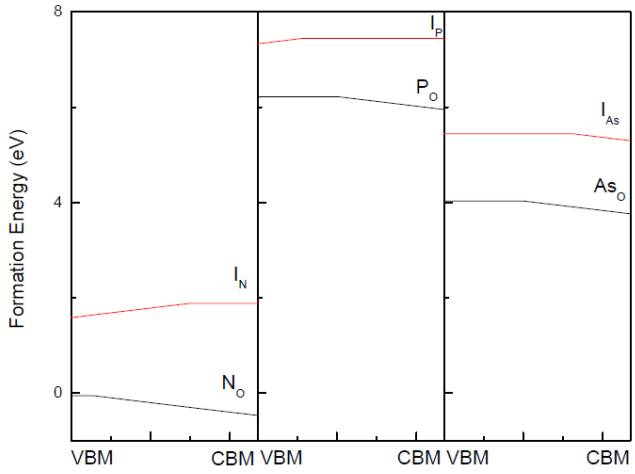

Figure 5.1 The formation energies of the group V dopants. In this figure, the formation energies of the substitutional defect in Cu_2O at the basic solution-growth environment of pH=9 are plotted, respectively. They vary with the Fermi level ranging from the valence-band maximum (VBM) to the conduction-band minimum (CBM). The lowest formation energies of interstitial site for each dopant are shown in their corresponding panels.

To compare the formation energies of different sites, only GGA are used due to the high cost of HSE calculations. The formation energies of these group V dopants by GGA are plotted

versus the Fermi level in the band gap, as shown in Figure 5.1. For each dopant at a specific site, only the lowest charge-state is drawn. Compared to interstitial defects, substitutional defects have much lower formation energies for all the three dopants. Therefore, the dopants are more stable on the substitution site in Cu_2O. Among these three group V elements, N has the lowest formation energy.

After eliminating the interstitial sites due to their much higher formation energies than those of the substitutional sites, more accurate and time-consuming HSE calculations are constructed for N_O, P_O, and As_O. The results obtained by HSE are shown in Figure 5.2. As it shows, the trend of the formation energies of the three dopants is the same as that in the GGA calculations.

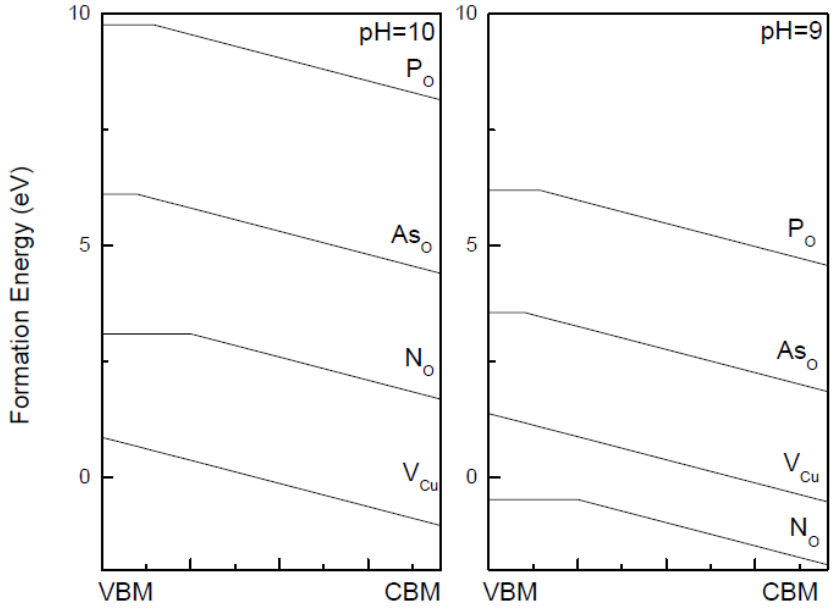

Figure 5.2 The formation energies of substitutional defects at the basic solution-growth environment of pH=9 and pH=10 are plotted. They vary with the Fermi level ranging from the valence-band maximum (VBM) to the conduction-band minimum (CBM). The lowest formation energies of interstitial site for each dopant are shown in their corresponding panels. The formation energy of the p-type native defect, Cu vacancy, is shown for comparison.

In Figure 5.2, the formation energy of V_{Cu} is shown for comparison. V_{Cu} is a dominant p-type native defect. To increase the conductivity of intrinsic Cu_2O, the formation energy of the

dopant has to be lower than that of V_{Cu} so that the defect of dopant will have higher concentration than V_{Cu}. As Figure 5.2 shows, at pH=10, the formation energies of all dopants are much higher than that of V_{Cu}, which means that the dopant has low concentration and that incorporation of dopant does not have a strong effect on conductivity of the copper oxide. When the pH is lowered to 9, the formation energy of N dopant becomes lower than that of V_{Cu}, and the concentration of dopant will increase. Among the three group V elements, N has the lowest formation energy. The formation energy of As is higher, 4.03 eV at the conduction band minimum. And P has the highest, though still at a reasonable value of 6.22 eV at the bottom of conduction band. The formation energy of N is below 0 eV. The formation energy of V_{Cu} is 1.59 eV higher than that of N dopant. Therefore, N doping is preferred to form than Cu vacancy. The high concentration of N_O should provide a large amount of holes, which will improve the conductivity of Cu_2O. This can explain Ishizuka's [112] experiment that why N doped Cu_2O increase the conductivity compared undoped Cu_2O.

5.6 Summary

The p-type doping by group V atoms in Cu_2O from different basic solution environment with pH=9 and pH=10 has been studied by the first-principles calculations. The calculated formation energies show that the dopants are more stable in the substitution sites than the interstitial sites due to the lower formation energies. The dopants present a p-type conduction behavior. However, the formation energies of P_O and As_O are still higher than that of V_{Cu} in both pH values, which mean that they are not dominant defects compared to V_{Cu} and have low concentration. At pH=9, the formation energy of N_O is lower than that of V_{Cu}, which means that N_O is a dominant defect with high concentration and provide more holes, and further improve the conductivity of Cu_2O. From the consideration of both the formation energy and the donor level, N is the best dopant among these three dopants at pH=9. At pH=10, the doping cannot improve the conductivity of native Cu_2O.The results are in good agreement with the very recent experimental results [112].

CHAPTER 6

N-TYPE DOPING IN ZINC OXIDE BY YTTRIUM

6.1 Introduction

Zinc Oxide (ZnO) mostly exists as the wurtzite form, which is most stable structure. Another form called zincblende can be obtained by growing ZnO on substrates with cubic lattice structure, but it is less stable. Therefore, the wurtzite structure is used for calculation in our research. Intrinsically, ZnO is an n-type semiconductor with a 3.4 eV direct band gap [115]. ZnO can be used as a popular transparent conducting oxide (TCO) [116], which offers low resistivity and high transmittance. Its source materials, Zn and O, are naturally abundant. Also, Zn and O are non-toxic. All of these advantages make ZnO an ideal material for TCO in terawatt-scale solar cells. ZnO can be used as the anti-reflective (AR) coating [117] on the top surface of the solar cell.

The most important features for ZnO as an AR coating are low resistance and high transmittance [117-118]. To further decrease the resistivity, doping is used to bring down the resistivity of ZnO to low 10-4 $\Omega \cdot \mathrm{cm}$ as required for AR coating and back reflector [119] in solar cells. Here, we consider a Group IIIB element, yttrium (Y), as an n-type candidate dopant in ZnO. Y is an abundant element and its reserve on the planet is 610,000 tons [116], which is helpful for large scale production of solar cell. Theoretically, Y has one more valence electron than Zn, which will provide extra free carriers and improve the conductivity. Experimentally, X. Han [120] and S. H. Mohamed [121] have proved this. We study the effect of Y doping in ZnO by using the first principles. In our research, the total energy calculations and the geometry optimizations have been carried out using density functional theory (DFT) and GGA-PBE functional [64] for exchange and correlation.

6.2 Computational Details

All the present calculations were performed using the VASP package [37-41] based on the Kohn-Sham formulism of density-functional theory (DFT). PAW method [95] was used to

describe the electron-ion interactions. The PAW potential for Zn was generated from the atomic configuration of $[Ar]3d^{10}4s^2$. For O, the atomic configuration to generate the PAW potential was $[He]2s^2 2p^4$. For Y, the atomic configuration to generate the PAW potential was $[Kr]3d^1 4s^2$. The geometry optimization, the total energy and the final electronic structure calculations are conducted using GGA-PBE approach. The comparison between our results and experimental values are shown in Table 6.1. The lattice constants we obtained are very close to the experimental value. However, the calculation value of Eg is well below the real value. This is because GGA underestimates Eg in general.

Table 6.1 Calculated lattice parameters a, c/a, and band gap Eg by using GGA and LDA.

	Calculation value by GGA	Experimental value
a (Å)	3.26	3.25 [123]
c/a	1.60	1.60 [123]
Eg (eV)	0.8	3.4 [123]

6.3 Calculation of Formation Energies

We begin our calculations with Y-doped ZnO bulk for which a 2X2X2 supercell consisting of 16 Zn atoms and 16 O atoms was used with k-point sampling of 4X4X4. Here, the defects considered include O vacancy (V_O) and Zn interstitial (I_{Zn}), and Y substitution of Zn (Y_{Zn}). V_o and I_{Zn} are two kinds of defects in ZnO which can provide the n-type conductivity. As Zhang's [122] paper reported, typically, the n-type conductivity of ZnO is provided by V_O due to its low formation energy. The formation energy of a V_O can be expressed as

$$\Delta H^f(V_O) = E(V_O) - E(P) + \mu_O + q[E_{VBM} + \varepsilon_F] \qquad (6.3.1)$$

where V_O represents one oxygen vacancy in ZnO. $E(V_O)$ is the total energy of the defect supercell with an O vacancy and $E(P)$ is the total energy of the perfect cell. μ_O is the chemical potential of an O atom.

The interstitial of Zn (I_{Zn}) is another n-type defect which will possibly provide the conductivity. However, its formation energy is higher than that of V_O. In this chapter, I_{Zn} is still considered. The formation energy of I_{Zn} defect can be expressed as

$$\Delta H^f(I_{Zn}) = E(I_{Zn}) - E(P) - \mu_{Zn} + q[E_{VBM} + \varepsilon_F] \qquad (6.3.2)$$

where I_{Zn} represents that one Zn atom goes into an interstitial site in ZnO.

Next, we try to calculate the formation energy of a substitutional yttrium (Y_{Zn}), which can be expressed as

$$\Delta H^f(Y_{Zn}) = E(Y_{Zn}) - E(P) + \mu_{Zn} - \mu_Y + q[E_{VBM} + \varepsilon_F] \qquad (6.3.3)$$

where Y_{Zn} represents that one yttrium atom replaces one zinc atom in ZnO. $E(Y_{Zn})$ is the total energy of the defect supercell doped by a Y atom and $E(P)$ is the total energy of the perfect cell. μ_{Zn} and μ_Y are the chemical potential of Zn atom and Y atom, respectively.

In this chapter, our focus is on the n-type doped ZnO by Y. We considered the formation energy of defects from two limit conditions, which are Zn-rich and O-rich. The chemical potential of metal Zn is used as the chemical potential of Zn. First, we begin to calculate the chemical potential of Y, which usually exists as a form of Y_2O_3. The total energy of Y_2O_3 can be obtained by calculation in VASP. According to the following equation, the chemical potential of Y can be calculated.

$$2\mu_Y + 3\mu_O = \mu_{Y_2O_3} \qquad (6.3.4)$$

Based on the above data, the formation energies of the three defects in ZnO as a function of the Fermi level, which varies from valence band maximum (VBM) to the conduction band minimum (CBM), are shown in Figure 6.1. Only the lowest-energy states are shown.

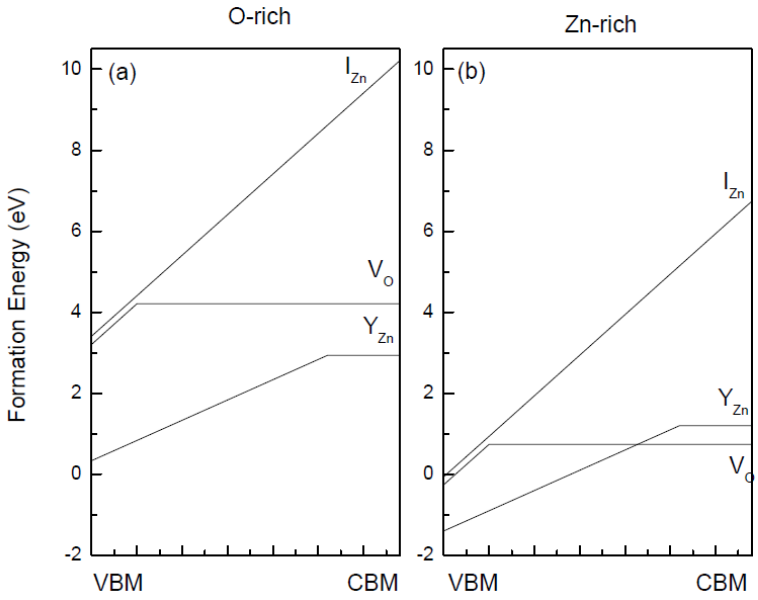

Figure 6.1 Formation energies of defects in ZnO under (a) O-rich and (b) Zn-rich conditions in vacuum based growth. The zero point of the Fermi level corresponds to the top the of the valence band. Only the lowest-energy charge states are shown.

Figure 6.1(a) shows the calculated formation of the n-type defects under the O-rich condition. Y_{Zn} has the lowest formation energy at conduction band minimum. The formation energy of V_O is higher than that of Y_{Zn} and a very deep transition level. I_{Zn} has the highest formation energy, which means that I_{Zn} is difficult to form and its concentration is very low. This trend verifies our initial assumption and experimental results [120-121]. Therefore, the doping of Y is preferred to form and the electron it provided will be excited to the conduction band minimum and further improve the conductivity of ZnO.

Figure 6.1(b) shows the formation energies under Zn-rich condition. In this condition, IZn still has the highest formation energy, compared to the other two defects. The difference between the formation energy of Y_{Zn} and V_O are very small, which means that both defects are dominant defects in this condition. However, the conductivity is mainly provided by Y_{Zn} due to the shallower transition level. Due to high concentration of V_O, the mobility of free electrons will be scattered by V_O. Therefore, Y doping cannot significantly improve the conductivity in Zn-rich

condition.

The (+1/0) transition levels for Y_{Zn} and V_O are 0.80 eV, and 2.90 eV below the conduction band minimum, respectively. Comparatively, Y_{Zn} has the shallower transition level. For I_{Zn}, the charge state is more stable than the neutral state across the band gap. Once it forms, the extra electron will easily go to the conduction band with absorbing lowest photon energy. In our study, Y_{Zn} has the lowest formation energy, which will be a dominant defect at O rich condition. And Y_{Zn} will improve the conductivity and lower the resistivity of ZnO. This is in a good agreement with the experiment [120-121].

6.4 Summary

In this chapter, n-type doped ZnO by Y is studied by first principles method in either O-rich or Zn-rich condition. In O-rich condition, Y_{Zn} has the lowest formation energy than $_{VO}$ and I_{Zn}. This will lead Y_{Zn} dominant defect and improve the conductivity. In Zn-rich, both Y_{Zn} and VO have a high concentration. However, the mobility of the electron provided by Y_{Zn} will be affected by V_O. Therefore, Y doping cannot significantly improve the conductivity in Zn-rich condition.

CHAPTER 7

CONCLUSION

Native point defects in pure Cu_2O have been studied by Density Functional theory with GGA and HSE hybrid functionals. The formation energies of native defects are calculated in two conditions, which are vacuum-based condition and solution-based condition. Copper vacancy has the lowest formation energy in vacuum based conditions, which provides p-type conductivity in Cu_2O. In the solution environment, n-type Cu_2O is achievable under strong acidic conditions, where the antisite defect CuO is the dominant charged defect and responsible for the n-type conduction. The theoretical results are in good agreement with experimental results [22, 107]. However, the resistivity of native n-type and p-type Cu_2O is still high.

To generate more carriers and improve the conductivity, doping in Cu_2O is studied. First, the n-type doping in Cu_2O is studied. Two different types of dopants are used, which are halogen atoms and selected metal atoms. The halogen atoms, which include F, Cl, and Br, is used to substitute the O atom. The selected metal atoms used include Zn, Ca, and Mg. They are used to substitute the Cu atom.

First, the n-type doping by halogens in the Cu_2O synthesized from an acidic solution environment has been studied by the first-principles calculations. From the view of formation energy, the dopants of F, Cl, and Br are most stable in the site of the substitutional sites of the O atoms than the interstitial sites. All these dopants present an n-type conduction behavior. Among them, the Cl atom has low formation energy and the shallowest donor level of 0.17 eV below the bottom of the conduction bands. From the consideration of both the formation energy and the donor level, the Cl is the best dopant among the three halogen atoms. The bottom of conduction band has substantial oxygen 3s and copper 4s orbitals, which are non-localized.

After the electron excited into the conduction band, it will improve the conductivity. The results are in good agreement with the very recent experimental results.

Another alternative doping is to substitute Cu by two-valence metal atoms. This type of doping is studied in solutions with different pH value to make sure that successful doping in Cu_2O can be obtained. The pH=6 is chosen for Zn while pH=4 is chosen for Ca and Mg. The calculated formation energies show that the dopants prefer to stay in the substitution sites due to the low formation energies. The dopants present an n-type conduction behavior. Among these three metal atoms, Ca has the shallowest donor level, only 0.11 eV below the bottom of the conduction bands. From the consideration of both the formation energy and the donor level, Ca is the best dopant among the three. After the electron excited into the conduction band, it will improve the conductivity. We hope that our findings will encourage experimental study aimed at n-type doped Cu_2O by metallic atoms.

Co-doping of Cl and Ca in Cu_2O is also studied. The chemical potentials of elements at pH=4 are used. The formation energy of the co-doping is not affected by the distance between these two dopants. From the view of the number of electrons provided by the defect, one co-doping defect is equivalent to combination of one Cl_O and Ca_{Cu}. The formation energy between co-doping and single doping are compared. It is concluded from our calculation that the formation energy of co-doping is smaller than the total formation energy of one Cl_O and one Ca_{Cu}, which means that co-doping is preferred to form when providing same number of electrons.

Next, the p-type doping by group V atoms in Cu_2O in a basic solution environment has been studied by the first-principles calculations. Here, pH=10 is finally chosen, which is the best condition for p-type doping to form according to our study. The calculated formation energies show that the dopants prefer stay in the substitutional sites of O atoms. The dopants present a p-type conduction behavior. However, compared to the formation energy of V_{Cu}, P and As have larger formation energies than V_{Cu}. This makes the doping of P and As difficult, which lead the

much lower concentration of P_O and As_O than that of V_O. Therefore, there is no significant improvement by doping. Only N_O has lower formation energy than V_{Cu}, which means that only N_O is a dominant defect and improve the conductivity. Therefore, N is the best dopant among the three group V elements. The results are in good agreement with the recent experimental results [112].

Finally, n-type doped ZnO by Y is studied. ZnO, with a 3.4 eV band gap and abundant source materials, is a good candidate material for transparent conducting oxide. To lower its resistivity, Y doping in ZnO is studied in either O-rich or Zn-rich condition. In O-rich condition, Y_{Zn} has the lowest formation energy than V_O and I_{Zn}. This will lead Y_{Zn} to be the dominant defect and improve the conductivity. In Zn-rich, both Y_{Zn} and V_O have a high concentration. However, the mobility of the electron provided by Y_{Zn} will be affected by the V_O.

REFERENCES

[1] Source: International Energy Agency Energy Statistics.

[2] Paul Mann, Lisa Gahagan, and Mark B. Gordon, American Association of Petroleum Geologists, 50 (2009).

[3] Dr. Irene Novaczek. "Canada's Fossil Fuel Dependency". Elements. Retrieved 2007-01-18.

[4] EPA. Archived from the original on March 12, 2007. Retrieved 2007-01-18.

[5] Renewables: Global Status Report (2011)

[6] Lars Kroldrup, Gains in Global Wind Capacity Reported Green Inc., (2010).

[7] James Russell, Record Growth in Photovoltaic Capacity and Momentum Builds for Concentrating Solar Power Vital Signs, (2010).

[8] Renewables Global Status Report, Update 12 (2009).

[9] K. A. Tsokos, "Physics for the IB Diploma", Fifth edition, Cambridge University Press, Cambridge, 2008.

[10] Perlin, John (2004). "The Silicon Solar Cell Turns 50". National Renewable Energy Laboratory. Retrieved 5 October 2010.

[11] J. Zhao, A. Wang and M. A. Green, Prog. Photovolt: Res. Appl., 7, 471 (1999).

[12] M. J. Keevers and M. A. Green, J. Appl. Phys., 75, 4022, (1994).

[13] W.Wang, O. K. Varghese, C. Ruan, M. Paulose, and C. A. Grimes, J. Mater. Res., 18 2756(2003)

[14] F. Marabelli, G. B. Parravicini, and F. Salghetti-Drioli, Phys. Rev. B, 52, 1433 (1995).

[15] J. N. Nian, C. C. Hu, H. Teng, Int. J. Hydrogen Energy, 33. 2897 (2008).

[16] D. Trivich, E. Y. Wang, and R. J. Komp, F. Ho, Conference Records of 12th IEEE Photovoltaic Specialists Conference , p. 875 (1976).

[17] A. E. Rakhshani, Solid-State Electron, 29, 7 (1986).

[18] N. A. Economou, R. S. Toth, R. J. Komp, and D. Trivich, in Proceedings of International Conference on Photovoltaic Solar Energy (Luxembourg, Reidel, 1977), p. 1180.

[19] Y. Zhou and J. A. Switzer, Scripta Mater. 38, 1731 (1998).

[20] A. Mittiga, E. Salza, F. Sarto, M. Tucci, and R. Vasanthi, Appl. Phys. Lett., 88, 163502 (2006).

[21] L. C. Olsen, F. W. Addis, and W. Miller, Sol. Cells, 7, 247 (1982).

[22] W. Siripala and J. R. P. Jayakody, Sol. Energy Mater., 14, 23 (1986).

[23] L. Wang and M. Tao, Electrochem. Solid-State Lett., 10, H248 (2007).

[24] W. Wang, D. Wu, Q. Zhang, L. Wang, and M. Tao, J. Appl. Phys., 107, 123717 (2010).

[25] X. Han, K. Han, and M. Tao, Electrochemical and Solid-State Letters, 12, H89-H91 (2009).

[26] S. N. Kale, S. B. Ogale, S. R. Shinde, M. Sahasrabuddhe, V. N. Kulkarni, R. L. Greene, and T. Venkatesan, Appl. Phys. Lett., 82, 2100 (2003)

[27] K. Ramamoorthy, C. Sanjeeviraja, M. Jayachandran, K. Sankaranarayanan, P. Misra, and L.M. Kukreja, Mater. Sci. Semi. Process, 6, 219 (2003).

[28] R.G. Gordon, MRS Bull., 25, 52 (2000).

[29] US Geological Survey, Mineral Commodity Summaries, US Government Printing Office, Washington (2008).

[30] A. Tsukazaki, A. Ohtomo, T. Onuma, M. Ohtani, T. Makino, M. Sumiya, K. Ohtani, S.F. Chichibu, S. Fuke, Y. Segawa, H. Ohno, H. Koinuma, and M. Kawasaki, Nature 4, 42 (2005).

[31] H.J. Ko, Y.F. Chen, S.K. Hong, H. Wenisch, T. Yao, and D.C. Look, Appl. Phys. Lett., 77, 3761 (2000).

[32] X. Han and M. Tao, IEEE Photovoltaic Specialists Conference, Proceedings 000305 (2010).

[33] S. H. Mohamed, M. El-Hagary, M. Emam-Ismail, J. of Natural Sciences and Mathematics, Qassim University, 3, 97 (2010).

[34] S. Ishizuka, S. Kato, T. Maruyama, K. Akimoto, Jpn. J. Appl. Phys., 40, 2765 (2001).

[35] P. Hohenberg and W. Khon, Phys. Rev., 136, B864 (1964).

[36] W. Kohn and L. J. Sham, Phys. Rev., 140, A1133 (1965).

[37] G. Kresse and J. Hafner, Phys. Rev. B, 47, 558 (1993).

[38] G. Kresse and J. Hafner, Phys. Rev. B, 49, 14251 (1994).

[39] G. Kresse and J. Furthmüller, Phys. Rev. B, 54, 11169 (1996).

[40] G. Kresse and J. Furthmüller, Comput. Mater. Sci., 6, 15 (1996).

[41] G. Kresse and D. Joubert, Phys. Rev. B, 59, 1758 (1999).

[42] J. Heyd, G.E. Scuseria, and M. Ernzerhof, J. Chem. Phys., 118, 8207 (2003).

[43] J. Heyd, G.E. Scuseria, and M. Ernzerhof, J. Chem. Phys., 124, 219906 (2006).

[44] Smil, V. 1990. “Missing energy perspectives”.

[45] Y. Abdu and A.O. Musa, Bajopas, 2, 2 (2009).

[46] Gordon E. Moore, (1965). Electronics Magazine, 4 (2006).

[47] National Renewable Energy Laboratory.

[48] M. Born and R. Oppenheimer, Annalen der Physik, 84, 457 (1927).

[49] D. R. Hartree, Proc. Cam. Phil. Soc., 24, 89 (1928).

[50] Zhiping Yin, UC Davis Ph.D. Doctoral Thesis (2009).

[51] M. Born and K. Huang, Dynamic Theory of Crystal Lattices, Oxford University Press (1954).

[52] L. H. Thomas, Proc. Cambridge Phil. Roy. Soc., 23, 542 (1927).

[53] E. Fermi, Rend. Accad. Naz. Lincei, 6, 602 (1927).

[54] P. A. M. Dirac, Proc. Cambridge Phil. Roy. Soc., 26, 376 (1930).

[55] M. Levy, Proc. Nat. Acad. Sci. USA, 76, 6062 (1979).

[56] U. von Barth and L. Hedin, J. Phys. C: Solid State Phys., 5, 1629 (1972).

[57] D. M. Ceperley and B. J. Alder, Phys. Rev. Lett., 45, 566 (1980).

[58] S. H. Vosko, L. Wilk and M. Nusair, Can. J. Phys., 58, 1200 (1980).

[59] J. P. Perdew and A. Zunger, Phys. Rev. B, 23, 5048 (1981).

[60] L. A. Cole and J. P. Perdew, Phys. Rev. A, 25, 1265 (1982).

[61] J. P. Perdew and Y. Wang, Phys. Rev. B, 45, 13244 (1992).

[62] A. D. Becke, Phys. Rev. A, 38, 3098 (1988).

[63] J. P. Perdew, J. A. Chevary, S. H. Vosko, K. A. Jackson, M. R. Pederson, and C. Fiolhais, Phys. Rev. B, 46, 6671 (1992).

[64] J. P. Perdew, K. Burke, and M. Ernzerhof, Phys. Rev. Lett., 77, 3865 (1996).

[65] A. D. Becke, J. Chem. Phys. 85, 7184 (1986)

[66] A. D. Becke, J. Chem. Phys., 98, 1372 (1993).

[67] A. D. Becke, J. Chem. Phys., 98, 5648 (1993).

[68] C. Lee, W. Yang, and R. G. Parr, Phys. Rev. B, 37, 785 (1988).

[69] S. H. Vosko, L. Wilk, and M. Nusair, Can. J. Phys., 59, 1200 (1980).

[70] J. Perdew and M. Enzerhof, J. Chem. Phys., 105, 9982 (1996).

[71] J. Heyd and G. E. Scuseria, J. Chem. Phys., 121, 1187, (2004).

[72] J. E. Peralta, G. E. Scuseria, and R. L. Martin, J. Chem. Phys., 123, 174101 (2005).

[73] M. Payne, M. Teter, D. Allan, T. Arias, and J. Joannopoulus, Rev. Mod. Phys., 64, 1045 (1992).

[74] N. Ashcroft, and N. Mernin, Solid State Physics, 133 (1976).

[75] M. Cohen, and V. Heine, Solid State Phys., 24, 37 (1970).

[76] M. T. Yin and Marvin L. Cohen, Phys. Rey. B, 25. 7403 (1982).

[77] D. Hamann, M. Schlüter, and C. Chiang, Phys. Rev. Lett., 43, 1494 (1982).

[78] Chris G. Van de Walle and Jörg Neugebauer, J. Appl. Phys., 95, 3851 (2004)

[79] David O. Scanlon, Benjamin J. Morgan, and Graeme W. Watson, J. Chem. Phys., 131, 124703 (2009)

[80] R. M. Nieminen, Topics in Applied Physics (Springer, New York, 2007)

[81] A.E. Rakhshani, Solid-State Electron., 29, 7 (1986).

[82] C. H. Henry, J. Appl. Phys., 51, 4494 (1980).

[83] F. Chaffar Akkari, M. Kanzari, and B. Rezig, Eur. Phys. J. Appl. Phys., 40, 49 (2007).

[84] V. Figueiredo, E. Elangovan, G. Gonc¸alves, N. Franco, E. Alves, S. H. K. Park, R. Martins, and E. Fortunato, Phys. Status Solidi A, 9, 2143 (2009).

[85] Y. Abdu and A.O. Musa, Bayero J. Pure and Appl. Sciences, 2, 2 (2009)

[86] Z. G. Yin, H. T. Zhang, D. M. Goodner, M. J. Bedzyk, R. P. H. Chang, Y. Sun, and J. B. Ketterson, Appl. Phys. Lett., 86, (2005) 061901.

[87] R.S. Toth, R. Kilkson, and D. Trivich, J. Appl. Phys., 31, 1117 (1960).

[88] M. O'Keeffe and W.J. Moore, J. Chem. Phys., 35, 1324 (1961).

[89] H.L. McKinzie and M. O'Keeffe, Phys. Lett. A, 24, (1967) 137.

[90] J. Ghijsen, L.H. Tjeng, J. van Elp, H. Eskes, J. Westerink, G.A. Sawatzky, and M.T. Czyzyk, Phys. Rev. B, 38, 11322 (1988).

[91] Kunhee Han and Meng Tao, Sol. Energy Mater. Sol. Cells, 93, 153 (2009).

[92] David O. Scanlon and Graeme W. Watson, J. Phys. Chem. Lett., 1, 2582 (2010)

[93] Hannes Raebiger, Stephan Lany, and Alex Zunger, Phys. Rev. B, 76, 045209 (2007)

[94] Ralph W G Wyckoff, Crystal structures.

[95] P.E. Blöchl, Phys. Rev. B, 50, (1994) 17953.

[96] A. F. Wright and J. S. Nelson, J. Appl. Phys., 92, 5849 (2002)

[97] M. Nolan and S. D. Elliot, Phys. Chem. Chem. Phys., 8, 5350 (2006)

[98] Kevin P. Driver, Ohio State University Ph.D. Thesis (2011).

[99] A. Werner and H. D. Hochheimer, Phys. Rev. B, 25, 5929 (1982)

[100] R. Garuthara and W. Siripala, J. Lumin., 121, 173 (2006).

[101] M. Fujinaka and A. A. Berezin, J. Appl. Phys., 54, 3582 (1983).

[102] P. E. de Jongh, D. Vanmaekelbergh, and J. J. Kelly, J. Electrochem. Soc., 147, 486 (2000).

[103] M. Zouaghi, M. Tapiero, J. P. Zielinger, and R. Burgraf, Solid State Commun. 8, 1823 (1970).

[104] D. O. Scanlon, B. J. Morgan, and G. W. Watson, Phys. Rev. Lett., 103, 096405 (2009).

[105] D. O. Scanlon, B. J. Morgan, and G. W. Watson, J. Chem. Phys., 131, 124703 (2009)

[106] M. Nolan, S. D. Elliott, Phys. Chem. Chem. Phys., 8, 5350 (2006).

[107] Kunhee Han and Meng Tao, Sol. Energy Mater. Sol. Cells, 93, 153 (2009).

[108] Xiaofei Han, Kunhee Han, and Meng Tao, Thin Solid Films, 518, 5363 (2010)

[109] S. N. Kale, S. B. Ogale, S. R. Shinde, M. Sahasrabuddhe, V. N. Kulkarni, R. L. Greene, and T. Venkatesan, Appl. Phys. Lett., 82, 2100 (2003).

[110] F. Atay, V. Bilgin, I. Akyuz, and S. Kose, J. Optoelectronics and Advanced Materials, 9, 3604 (2007).

[111] M. Nolan and S. D. Elliott, Chem. Mater., 20, 5522 (2008)

[112] Shogo Ishizuka, Shinya Kato, Takahiro Maruyama and Katsuhiro Akimoto, Jpn. J. Appl. Phys., 40, 2765 (2001)

[113] Yoshitaka Nakano, Shu Saeki, and Takeshi Morikawa, Appl. Phys. Lett., 94, 022111(2009).

[114] H.J. Li, C.Y. Pu, C.Y. Ma, Sh. Li, W.J. Dong, S.Y. Bao, and Q.Y. Zhang, Thin solid film 520 212 (2011).

[115] A. Tsukazaki, A. Ohtomo, T. Onuma, M. Ohtani, T. Makino, M. Sumiya, K. Ohtani, S.F. Chichibu, S. Fuke, Y. Segawa, H. Ohno, H. Koinuma, and M. Kawasaki, Nature 4, 42 (2005).

[116] US Government Printing Office, Washington (2008).

[117] K. Ramamoorthy, C. Sanjeeviraja, M. Jayachandran, K. Sankaranarayanan, P. Misra, and L.M. Kukreja, Mater. Sci. Semi. Process 6, 219 (2003).

[118] R.G. Gordon, MRS Bull. 25, 52 (2000).

[119] H. J. Ko, Y. F. Chen, S. K. Hong, H. Wenisch, T. Yao, and D.C. Look, Appl. Phys. Lett. 77, 3761 (2000).

[120] X. Han, and M. Tao, IEEE Photovoltaic Specialists Conference, Proceedings 000305 (2010).

[121] S. H. Mohamed, M. El-Hagary, and M. Emam-Ismail, J. Natural Sciences and Mathematics, Qassim University, 3, 97 (2010).

[122] S. B. Zhang, S. H. Wei, and Alex Zunger, Phys. Rev. B, 63, 075205 (2001).

[123] Semiconductors—Basic Data, 2nd revised ed., edited by O. Madelung (Springer, Berlin, 1996).

[124] H. Schulz and K. H. Thiemann, Solid State Commun., 23, 815 (1977).

[125] Gianni Taraschi, Mcgill University Ph.D. Thesis (1997).

[126] Qiong Bai, Weichao Wan, Qiming Zhang, and Meng Tao, J. Appl. Phys., 111, 023709 (2012)

BIOGRAPHICAL INFORMATION

Mr. Qiong Bai was born in 1985. He earned a Bachelor of Science degree majored in Materials Science and Engineering from Tianjin University, Tianjin, China in 2008 and in the same year, he joined the BS-PhD Bound Program in University of Texas at Arlington. He earned a Doctor of Philosophy degree in Materials science and Engineering at the University of Texas at Arlington in August 2012. During his study in the University of Texas at Arlington, his worked on the areas related to first-principles simulation on the n-type and p-type doping of metal oxides.